Archaeal SegAB forms a bipolar structure that promotes chromosome segregation in spherical cells

Arthur Charles-Orszag[1,2], Samuel J Lord[1], Nadia Herrera[3], Luke Strauskulage[4], Arghya Bhowmick[1], Tom Goddard[5], Bianca Wassmer[6], Marleen van Wolferen[6], Garrison Asper[1], Amy Flis[1], Johnny Rodriguez[1], Sy Redding[4,7], Oren Rosenberg[3], Sonja-Verena Albers[6], & R. Dyche Mullins[1,*]

[1] Department of Cellular and Molecular Pharmacology, Howard Hughes Medical Institute, University of California, San Francisco, San Francisco, CA, USA

[2] Department of Microbiology and Molecular Genetics, College of Biological Sciences, University of California Davis, Davis, CA, USA

[3] Department of Medicine, University of California San Francisco, San Francisco, California, USA

[4] Department of Biochemistry and Biophysics, University of California San Francisco, San Francisco, CA, USA

[5] Department of Pharmaceutical Chemistry, University of California San Francisco, San Francisco, CA, USA

[6] Molecular Biology of Archaea, Faculty of Biology, Institute of Biology II, University of Freiburg, Freiburg, Germany

[7] Department of Biochemistry and Molecular Biotechnology, University of Massachusetts Chan Medical School, Worcester, MA, USA

*Correspondence to R. Dyche Mullins (dyche.mullins@ucsf.edu)

Abstract

Archaeal *segAB* operons are thought to promote chromosome segregation, but their mechanism remains unknown. We employ comparative genomics, structural biology, genetic knockouts, and quantitative cell biology to investigate how SegA and SegB proteins work together to segregate chromosomes in the thermophilic archaeon *Sulfolobus acidocaldarius*. *In vitro*, SegB binds a centromeric DNA sequence adjacent to the *segAB* operon, and *in vivo* forms a distinct focus on each segregating chromosome. SegA, a ParA-like ATPase, binds DNA non-specifically *in vitro* and promotes chromosome compaction and segregation *in vivo*. During division, SegA shifts from chromosome-associated puncta to form a single, elongated figure that runs between separating SegB foci. Late in division, SegA retreats to regions surrounding separated SegB foci. Elongated SegA figures appear in *segB* knockout cells but no longer lie perpendicular to the division plane. We propose that SegA and SegB interact to form a bipolar, DNA-segregating structure radically different from bacterial ParABS systems.

Introduction

How do dividing cells distribute genetic material to their daughters? In eukaryotes, the microtubule-based mitotic spindle captures, aligns, and segregates chromosomes (Valdez et al., 2023). In bacteria and archaea, the situation is less clear. Many bacterial (and some archaeal) chromosomes contain partitioning (Par) operons that promote proper chromosome segregation. The most common partitioning operons in both bacteria and archaea rely on ParA-type ATPases (Merino-Salomón, Babl, and Schwille 2021; Pulianmackal et al. 2023). Work on ParA-based systems has yielded attractive models for bacterial DNA segregation, but archaeal variants remain mysterious (Lim et al. 2014).

ParA homologs are best understood in bacteria, where many of them function as components of ParABS segregation systems. These bacterial ParABS systems comprise (i) a centromeric DNA locus, *parS*; (ii) a centromere-binding protein, ParB; and (iii) an ATPase, ParA (Mohl and Gober 1997; Toro et al. 2008). The ParB protein forms a dimeric clamp that loads onto DNA specifically at the *parS* locus (Jalal et al. 2021; Osorio-Valeriano et al. 2019). The ParA protein binds nonspecifically to DNA, with an affinity regulated by its ATPase activity. In most species studied to date, ATP-ParA binds DNA more tightly than the ADP-bound form (Lim et al. 2014), and ParB promotes ParA dissociation by accelerating ATP hydrolysis (Easter and Gober 2002; Lim et al. 2014).

Recent models based on data from rod-shaped bacteria argue that ParABS promotes DNA segregation via a reaction-diffusion process. In these models, ParB/*parS* segregation complexes create a gradient of DNA-bound ParA by locally promoting ATP hydrolysis and dissociation from DNA (Chin Hwang et al. 2012). Experimentally, ParA disappears from regions surrounding ParB/*parS* complexes even before initiation of chromosome segregation is detectable (Surovtsev, Lim, and Jacobs-Wagner 2016). Once formed, the self-generated ParA gradient is thought to rectify random thermal motion of a mobile ParB/*parS* segregation complex, driving it on a journey from one cell pole to the other. In a version of this model called the DNA relay, ParB/*parS* movement is further assisted by the spring-like mechanics of chromosomal DNA (Lim et al. 2014). During this trip, the ParA gradient retreats toward the distal cell pole, just ahead of the steadily advancing ParB/*parS* complex. This picture is way less clear in

non-rod-shaped bacteria, and only recently was it reported that *Neisseria gonorrhoeae* ParB does not localize to the cell poles but rather aligns with the long axis of the cell during cytokinesis (Bandekar et al., 2025).

Some archaeal chromosomes contain genes encoding ParA-like proteins, but little is known about their function. Genomes of both *Saccharolobus solfataricus* (*Sso*) and *Sulfolobus acidocaldarius* (*Saci*), for example, encode an ATPase called SegA that shares ~34% sequence identity with bacterial ParA proteins. The gene immediately adjacent to *segA*, however, exhibits no sequence similarity to bacterial *parB*, and encodes an archaea-specific protein called SegB (Kalliomaa-Sanford et al. 2012). Both SegA and SegB are expressed in a cell cycle-dependent manner (Lundgren and Bernander, 2007), and overexpression or deletion of the *segAB* operon in both *Sso* and *Saci* produce growth defects, abnormal nucleoid morphology, and anucleate cells, consistent with a role in chromosome segregation (Kalliomaa-Sanford et al. 2012; Kabli et al. 2025). Additionally, *Sso*—but not *Saci*—encodes a second NTPase, SegC, that co-assembles into filaments with SegA and DNA *in vitro* (Lin et al., 2024). Structurally, the SegA protein from *Sso* resembles bacterial ParA, but with a variant dimer architecture (Yen et al. 2021), while the enigmatic SegC adopts a Thiamin diphosphate-binding fold (Lin et al. 2024). Unfortunately, only the C-terminal two thirds of the *Sso* SegB protein (residues 34-109) has been crystallized. This truncated SegB adopts a helix-turn-helix fold, forms dimers, and binds DNA—but it lacks the SegA-interacting N-terminal region (Yen et al. 2021).

Sequence analysis and comparative genomics reveal a correlation between the presence of a *segB* gene and spherical cell shape, suggesting that SegB evolved to help break cellular symmetry and establish an axis for chromosome segregation in non-rod-shaped archaea. But until now, no clear models have emerged for how SegA and SegB promote chromosome segregation. SegB binds multiple loci throughout the *Sso* chromosome, including the centromeric DNA sequence, *segS*, located upstream of the *segAB* operon (Kabli et al. 2025; Kalliomaa-Sanford et al. 2012; Yen et al. 2021). SegB in complex with DNA was proposed to form a superhelix that links distant chromosomal loci to form discrete SegB/DNA clusters throughout the cytoplasm of non-dividing cells, and to promote ATP hydrolysis by SegA (Kalliomaa-Sanford et al., 2012). Similar to bacterial ParA, SegA binds non-specifically to DNA but, unlike in bacteria, this binding does not appear to be regulated by ATP hydrolysis (Yen et al.

2021). First thought to assemble into short polymers (Kalliomaa-Sanford et al. 2012), SegA was later reported to form discrete foci in non-dividing cells, leading to the hypothesis that SegA and SegB combine genome organization and chromosome segregation activities (Kabli et al., 2025).

We chose to study the SegAB system in *Saci*, in part because the lack of SegC suggested that its mechanism might be simpler than that of *Sso*. We first crystallized full-length *Saci* SegB and solved its structure, which revealed a similar helix-turn-helix motif but a very different dimer architecture from that reported by Yen et al. (2021) for the truncated *Sso* SegB. *In vitro*, we find that SegB from *Saci* binds a specific sequence (*segS*), immediately upstream of the *segAB* operon and close to one of the three origins of replication. In non-dividing cells, SegB is minimally expressed and exhibits no clear localization pattern, but during division it forms two well defined chromosome-associated foci that eventually localize to opposite poles of the cell. In *segA*-knockout cells, SegB forms several foci, suggesting that SegA acts to limit or concentrate its localization.

SegA undergoes a more dramatic rearrangement during division. Mostly absent in non-dividing cells, SegA appears as chromosome-associated foci in early stages of division, but then forms an elongated, filament-like figure running between SegB foci as division progresses. In wildtype cells, this divisional SegA figure always runs perpendicular to the plane of cell division. Loss of SegB does not abrogate formation of this SegA figure, but randomizes its orientation with respect to the division plane. From these data, we propose a model for SegAB-mediated chromosome segregation completely distinct from the current understanding of the ParABS mechanism in bacteria.

Results

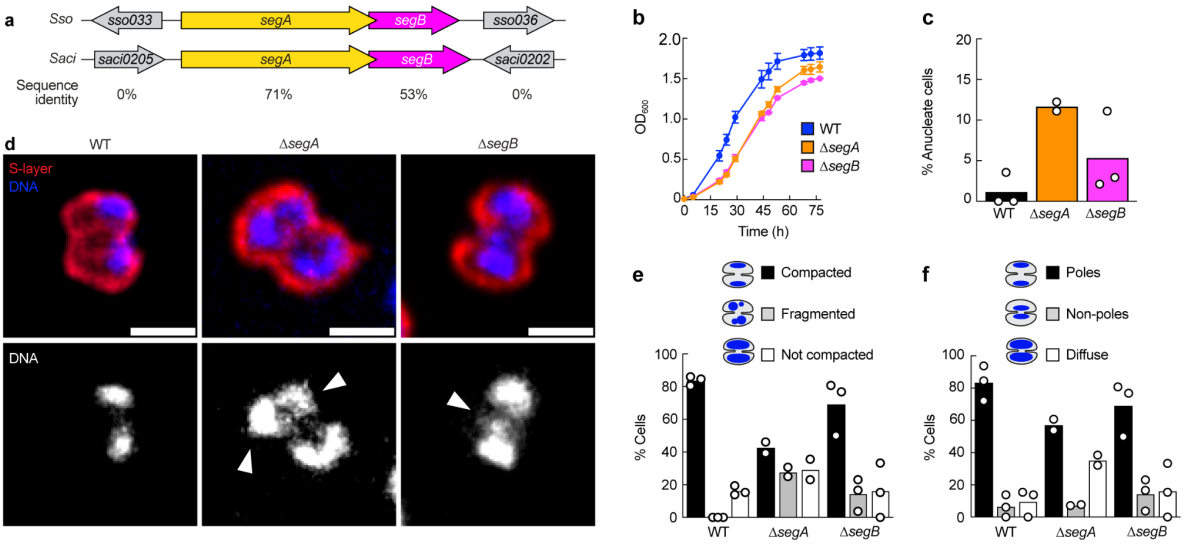

Figure 1. *S. acidocaldarius* SegAB promotes chromosome segregation and compaction. a. Comparison between the *segAB* operons of *Saccharolobus solfataricus* (Sso) and *S. acidocaldarius* (Saci). **b.** Growth of Δ*segA* and Δ*segB* deletion strains compared to WT. Data points represent the mean ±SEM of three technical replicates; representative of three biological replicates. **c.** Quantification of the absence of chromosomal DNA (anucleate) in WT, Δ*segA* and Δ*segB* deletion strains. **d.** Super-resolution fluorescence of chromosomal DNA in indicated strains. Arrowheads indicate fragmented chromosomes. Scale bars, 1 µm. **e, f.** Quantitative analysis of the aspect and localization of chromosomal DNA in WT, Δ*segA* and Δ*segB* cells. A total of 161 (WT), 81 (Δ*segA*) and 109 (Δ*segB*) cells were analyzed; each dot represents the mean of a biological replicate.

The *S. acidocaldarius* chromosome contains a *segAB* operon that promotes chromosome segregation

Genome analysis reveals that *S. acidocaldarius* (*Saci*) encodes homologs of both *segA* and *segB* genes (saci0204 and saci0203), originally described in *Sa. solfataricus* (*Sso*). The SegA and SegB proteins encoded by these *Saci* genes share 71% and 53% sequence identity with their *Sso* counterparts. Similar to Sso, the 3' region of the *Saci segA* gene overlaps the 5' region of *segB* (Kalliomaa-Sanford et al., 2012), suggesting that the two genes are transcribed as a single unit and likely function together in the same process (Wurtzel et al., 2010). The genomic context of the *segAB*

region of Saci differs significantly from that of *Sso* (Fig. 1a and 3c), indicating that *segA* and *segB* have maintained close proximity across evolutionary time scales and/or have moved together as a unit during lateral gene transfer events. While the SegA proteins from *Saci* and *Sso* are of similar size, the Saci SegB protein is almost 50% larger than the *Sso* version (151 versus 109 amino acids) (Fig. 1a and 3c). This difference illustrates the size range of archaeal SegB proteins, which can vary more than five-fold in length (Kabli et al., 2025; Kalliomaa-Sanford et al., 2012) from species to species (see below).

To understand the function of the *segAB* operon in *Saci* we created deletion strains for both *segA* and *segB*. Although viable, both mutant strains exhibited a significant growth defect compared to WT cells (Fig. 1b). Consistent with results from *Sso* (Kabli et al., 2025; Kalliomaa-Sanford et al., 2012), we also observed an increase in the number of anucleate cells in both knockout strains: increasing from 1.19%±2.06, in wildtype cells, to 11.68%±0.80 and 5.39%±4.9, in *segA* and *segB* knockouts respectively (Fig. 1c). To compare chromosome morphology and localization in wildtype and mutant strains, we fixed cells after covalently labeling the S-layer, stained DNA with DAPI, and imaged them by super-resolution (iSIM) light microscopy (Fig. 1d). We scored only cells undergoing division, as judged by asymmetric cell shape and the presence of detectable ingression of a cleavage furrow. To avoid observer bias we performed imaging and quantification double-blind. Chromosomes more often appeared fragmented in both *segA* and *segB* deletion strains (Fig. 1e, left graph). Interestingly, knocking out *segA* caused a bigger increase in the fraction of cells with uncompacted and diffusely localized chromosomes (Fig. 1e) than loss of *segB*. From these experiments we conclude that SegA and SegB promote chromosome segregation in *Saci*, and that SegA plays an additional role in compaction of segregating chromosomes.

Finally, we used high-temperature (76°C) time-lapse imaging to compare cytokinesis in wildtype and mutant cells. When we tracked visible cleavage furrow ingression, we saw no difference in the rate or duration of cytokinesis in the Δ*segB* strain compared with wildtype (Fig. S1 c, d). When we used mother-daughter cell separation as a marker for abscission, however, we noted a slight (statistically non-significant) delay in Δ*segB* cells (Fig. S1 e, f).

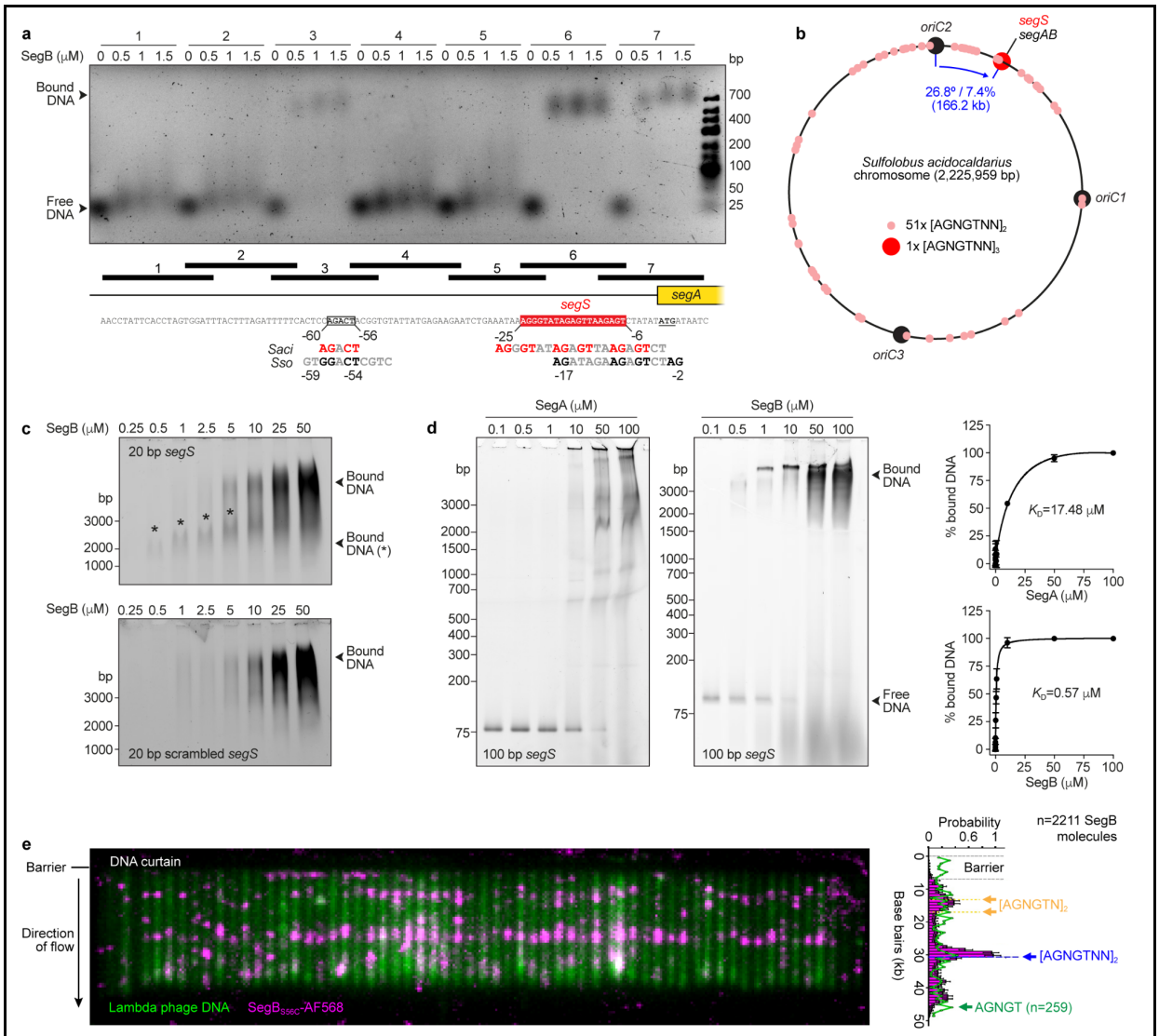

Figure 2. *Sulfolobus acidocaldarius* SegB binds centromeric DNA sequence, *segS*. a. Identification of the centromeric sequence and SegB binding partner *segS* upstream of the *segAB* operon by EMSA. Alignment with the corresponding region in Sso shows partial conservation of *segS*. **b.** Bioinformatic mapping of one full *segS* sequence (containing three repeats) and 51 shorter *segS*-like motifs onto Saci chromosome. **c.** EMSA showing binding of SegB to *segS* and scrambled DNA sequences. Asterisks indicate *segS*-specific binding. **d.** EMSA showing binding of SegA and SegB to a 100-bp DNA fragment corresponding to the 50-bp upstream and downstream of the *segAB* operon containing *segS*. The graphs represent the determination of SegA-DNA and SegB-DNA respective dissociation constants by densitometry in two independent experiments each. **e.** DNA curtain assay showing the binding of single molecules of $SegB_{S56C}$ labeled with AlexaFluor 568 to lambda phage

DNA under flow. The bar plot shows the distribution of all $SegB_{S56C}$ molecules imaged along lambda phage DNA. Single, double and near-double *segS* motifs present in the DNA are indicated. The highest binding peak corresponds to a double repeat of the *segS* motif.

Sequence-specific binding of SegB to sites in the *S. acidocaldarius* chromosome

For *in vitro* experiments, we expressed the full-length SegB protein fused to a SUMO (Small Ubiquitin-like Modifier) tag. Following purification, we cleaved and separated the SUMO tag to produce SegB with no additional amino acid residues on either the N- or C-terminus. The mobility of this purified SegB in gel electrophoresis (SDS-PAGE) assays was consistent with a molecular weight of 20 kDa, slightly higher than its predicted molecular weight of 17.4 kDa (Fig. S2). In addition to this wildtype SegB, we also created a fluorescent SegB derivative by mutating a surface-exposed serine residue (S56) to cysteine ($SegB_{S56C}$) and then reacting this mutant protein with a maleimide-functionalized fluorescent dye (AlexaFluor 568).

We used purified SegB and electrophoretic mobility shift assays (EMSAs) to look for specific binding sequences in the chromosomal region near the *segAB* operon (Fig. 2a and Fig. S2). SegB binds strongly to a 300-bp fragment immediately upstream of *segAB* but only weakly interacts with DNA oligonucleotides from the 3' flanking region (Fig. S2). We narrowed down the SegB binding site by splitting the proximal 100 base pairs on the 5' side of the *segA* start codon into 20-bp DNA fragments with 5-nucleotide overlaps (Fig. 2a). In these experiments SegB bound specifically to the two DNA fragments closest to *segA* start codon. From this we deduce that SegB binds specifically to the DNA sequence that runs from nucleotides -25 to -6 on the 5' side of the *segA* start codon (5'-AGGGTATAGAGTTAAGAGT-3'). Consistent with established nomenclature (Kalliomaa-Sanford et al., 2012), we refer to this sequence as the *Saci segS* motif. SegB-*segS* binding was sequence-specific as judged by EMSA assays performed using SegB and 20-bp DNA molecules containing either a native or scrambled *segS* sequence (Fig. 2c).

232 Unlike SegB, recombinant SegA binds DNA with no obvious sequence specificity (Fig.
233 2d and Fig. S2). By EMSA SegA binds with lower affinity (K_d=17.48 μM) than SegB
234 (K_d=0.57 μM) to a 100-bp DNA fragment containing the 50 base pairs upstream and
235 downstream of *segAB* (Fig. 2d).
236
237 *Saci segS* exhibits weak homology to the *segS* motif found in Sso (Fig. 2a) but, unlike
238 the Sso version, it does not form a pseudo-palindrome. Instead, *Saci segS* comprises
239 three repeats of the motif [AGNGTNN]. Interestingly, SegB also bound (although with
240 lower apparent affinity) to a third DNA fragment located -60 to -56 base pairs upstream
241 of *segA* start codon. This oligonucleotide contains an AGACT sequence reminiscent
242 of the three [AGNGTNN] repeats found in *segS*. The full-length *segS* (i.e. the triple
243 repeat $[AGNGTNN]_3$) occurs only once in the entire *Saci* chromosome, adjacent to the
244 *segAB* operon and 166.2 kb (7.6% of the genome size) from *oriC2* , one of three origins
245 of replications in *Saci* (Fig. 2b). For comparison, ~92% of bacterial *parS* sites fall within
246 15% of the chromosome length from *oriC*, the origin of replication in primary bacterial
247 chromosomes (Livny et al., 2007). Because we found that SegB can bind partial *segS*
248 motifs *in vitro* (Fig. 2c), we looked for additional incomplete *segS* motifs in the *Saci*
249 genome and found 51 double repeats ($[AGNGTNN]_2$) scattered across the
250 chromosome (Fig. 2b).
251
252 To assess the ability of SegB to bind partial and/or imperfect *segS* sequences, we
253 employed a single-molecule DNA curtain approach (Fig. 2e; Greene et al., 2010).
254 Briefly, we immobilized ~50 kbp molecules of double-stranded DNA from
255 bacteriophage λ in a microfluidic flow chamber, via a supported lipid bilayer. We
256 labeled the DNA molecules with the intercalating dye YOYO-1. We then pulsed
257 fluorescently labeled SegB protein into the flow chamber and imaged both DNA and
258 SegB by Total Internal Reflection Fluorescence (TIRF) microscopy. In this assay
259 labeled SegB binds predominantly to two regions in the lambda phage DNA, located
260 at ~15 kb and ~30 kb positions, with probabilities of ~40% and ~80% respectively (Fig.
261 2e). Little or no binding was observed outside of these loci, despite the presence of
262 259 AGNGT motifs separated by more than one base pair. Interestingly, the region
263 around 15 kb contains two $[AGNGTN]_2$ motifs, corresponding to two *segS*-like
264 sequences where two AGNGT sequences are separated by one base pair instead of

265 two, while the region around 30 kb contains one true [AGNGTNN]$_2$ *segS*-like sequence
266 as found throughout Saci chromosome (Fig. 2b).
267
268 Together, our DNA-protein interaction studies demonstrate that *Saci* SegA binds DNA
269 non-specifically, with potential to interact throughout the entire chromosome. In
270 contrast, SegB exhibits both sequence-specific and non-specific DNA binding. The
271 affinity of SegB for segS-like sequences composed of partial and/or imperfect repeat
272 motifs suggests that SegB may bind multiple partial and/or imperfect *segS* sites across
273 the chromosome in addition to the high-affinity *segS* site proximal to the *segAB*
274 operon.
275
276

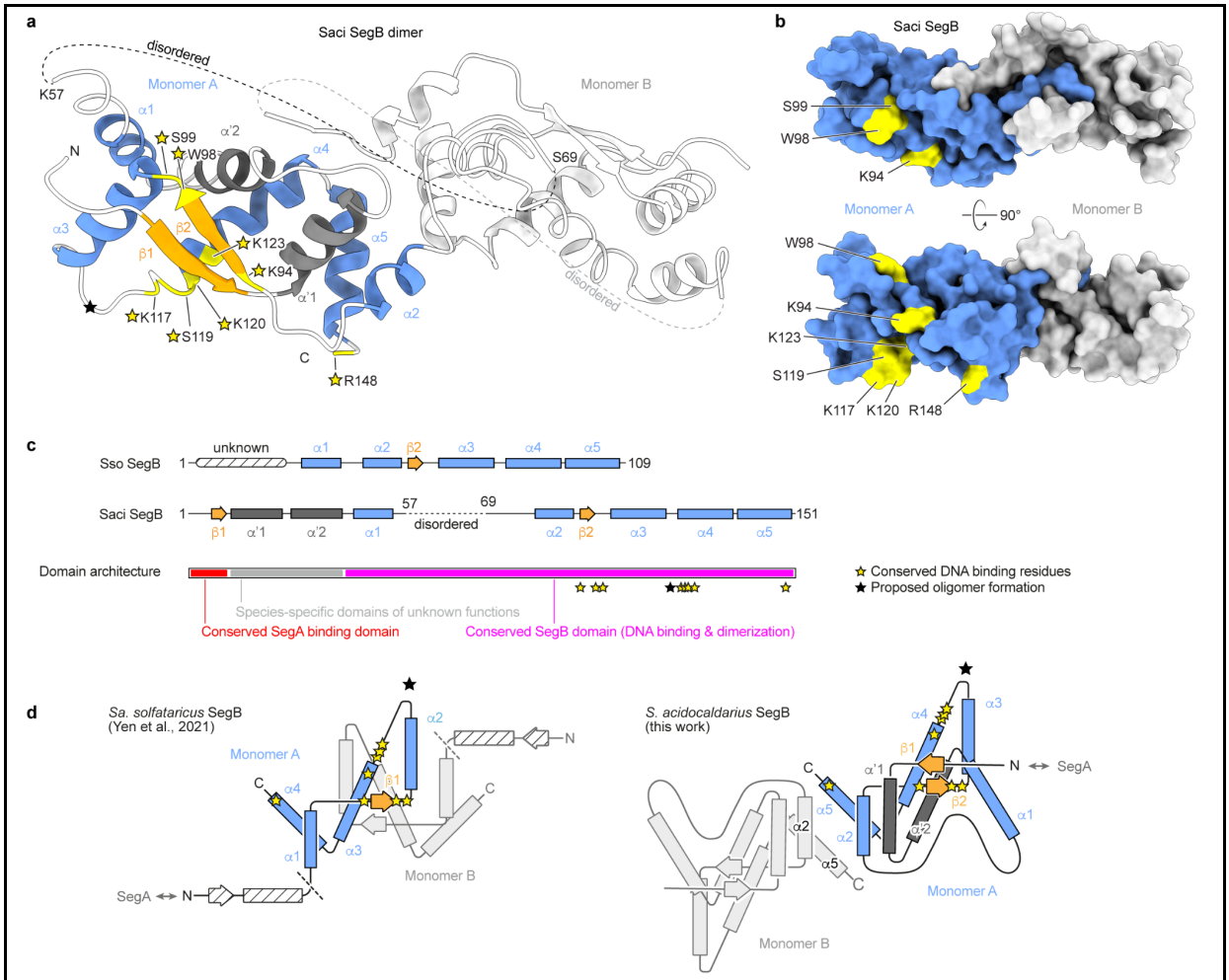

277
278 **Figure 3. Structure determination of SegB in *Sulfolobus acidocaldarius*. a.**
279 Ribbon diagram of Saci SegB dimer. In monomer A, conserved alpha helices are
280 colored in blue while helices specific to Saci are colored in dark gray. Conserved beta

strands are colored in gold. Gold stars indicate conserved residues involved in DNA binding, while the light grey star corresponds to the residue proposed to be involved in oligomer formation in Sso SegB. Monomer B is colored in light grey for clarity. **b.** Surface representation of Saci SegB dimer showing the head-to-tail dimer conformation and solvent accessibility of all the conserved residues involved in DNA binding. **c.** Secondary structure and domain organization of Saci and Sso SegB homologs. **d.** Comparison between the folding of truncated Sso SegB and full-length Saci SegB.

Structure of the *S. acidocaldarius* SegB dimer

SegB from *Saci* is considerably larger than its counterpart in *Sso* (151 versus 109 amino acids), with most of the difference down to two sequence insertions. One 30-residue insertion appears at a position equivalent to R12/K13 in *Sso* SegB and another, 12-residue insertion, occurs at N26/A27 of *Sso* SegB. Bioinformatic analyses fail to predict secondary structure for these insertions and their potential function is unknown. In addition, the previously determined structure of *Sso* SegB (Yen et al. 2021) is missing the N-terminal one third of the molecule (residues 1-33), which contains the SegA-interacting region. To fill these gaps, we crystallized full-length *Saci* SegB and solved its atomic structure at 1.85Å resolution (Fig. 3a). Consistent with previous structural work (Kalliomaa-Sanford et al., 2012; Yen et al., 2021) and our circular dichroism measurements (Fig. S1), SegB forms a dimer (Fig. 3a) of globular proteins, composed mostly of α-helices with a small percentage of β-strand and disordered regions (Fig. 3a). Comparing *Sso* and *Saci* structures reveals that all secondary structural elements of Sso SegB also appear in the *Saci* protein, namely the five alpha helices (α1 to α5) and the lone beta strand (β2).

The conserved N-terminal SegA-binding domain (Yen et al., 2021)—missing from the *Sso* SegB structure—contains an additional beta strand (β1), which contacts β2 to form an antiparallel sheet (Fig. 3a, d). While the region between residues K57 and S69 did not form a stable tertiary structure, the 30-residue insertion unique to *Saci* SegB forms two alpha helices (α'1 and α'2), arranged in a helix-turn-helix configuration. This arrangement enables β1 and β2 to interact while preserving the conserved ribbon-helix-helix motif formed by β2, α3 and α4 (β1, α2, α3 in *Sso* SegB, (Yen et al., 2021))

314 (Fig. 3c, d). All eight conserved residues involved in DNA binding, K94, W98, S99,
315 K117, S119, K120, K123 and R148 (corresponding to *Sso* K52, W56, S57, K75, S77,
316 K78, K81, R106), as well as residues proposed to be involved in oligomerization (Yen
317 et al., 2021) are exposed on the surface of the protein (Fig. 3a, b).
318
319 Surprisingly, the dimer architecture of *Saci* SegB differs strikingly from that reported
320 for the *Sso* protein (Fig. 3a, b, d). In SegB from *Sso*, dimerization involves the β1
321 strand from each monomer, interacting to form an antiparallel sheet (Fig. 3d) (Yen et
322 al., 2021). In our *Saci* SegB structure, two beta strands from the same polypeptide (β1
323 and β2) form an *intra*-molecular antiparallel sheet (Fig.3 a, d) similar to the *inter*-
324 molecular interaction reported for *Sso* SegB. The dimer interface in our structure is
325 formed by the α2 and α5 helices from each monomer (Fig. 3 a, d). To verify that our
326 structure for the *intra*-molecular beta sheet is correct, we inspected the electron
327 density of side chains in this region. Electron density maps showed clearly that the
328 sequences of the two interacting beta strands are different, representing β1 and β2
329 from the same polypeptide, rather two β1 strands from different polypeptides (Fig. S3).
330 Since the residues forming β1 in our structure were missing from the truncated *Sso*
331 SegB (Yen et al., 2021) we suggest that the N-terminal region of *Sso* SegB may also
332 contain an additional beta strand (Fig. 3d), and that full-length SegB from *Sso* may
333 also form a dimer similar to the one in *Saci*. In any case, it is remarkable that in *Saci*
334 SegB the central helix-turn-helix fold and the solvent accessibility of the residues
335 involved in binding to DNA are conserved despite the evolution of two additional non-
336 conserved N-terminal alpha helices.
337
338
339 **Sequence diversity and evolutionary history of archaeal SegB proteins**
340 The size difference between *Saci* and *Sso* SegB proteins inspired us to compare more
341 SegB homologs. We used the *Sso* SegB protein sequence as a query to the Basic
342 Local Alignment Search Tool (BLAST; (Altschul et al., 1990)), searching against the
343 entire NCBI non-redundant sequence database (see Materials and Methods). The
344 initial search returned 117 hits, but we winnowed this list by removing redundant or
345 incomplete sequences as well as sequences from unidentified or poorly annotated
346 species. We kept only sequences containing the signature, C-terminal SegB motif
347 (K/R-D/N-P-K/R-I-G/T-V/L-WS-Y/P-P/E), which left 72 unique sequences from well-

348 defined species (Fig. S4). All these sequences were adjacent to a predicted ParA-like
349 ATPase. Predicted SegB homologs fell into two clusters: a large group (50 sequences)
350 in the Thermoproteota and a smaller group (22 sequences) in the Euryarchaeota.
351 Thermoproteota sequences clustered into eight further subgroups, with pairwise
352 identities to *Sso* SegB as low as 39% (in *Sulfodiicoccus acidiphilus*). Euryarchaeota
353 sequences fell into four subgroups (Fig. S4a) with generally lower pairwise identities
354 to *Sso* SegB (from 30% in *Methanosphaera sp.* to 49% in *Thermococcus aggregans*).
355 The predicted length of SegB proteins varied from 68 to 331 amino acids, with most
356 homologs falling between 105-120 amino acids (Fig. S4b). The low degree of
357 conservation among SegB homologs largely reflects variability in the middle of the
358 polypeptides, a region that contains most of the species-specific features (Fig. S4c).
359 In contrast, the first 10-12 and last 60 amino acids are highly conserved across the
360 entire SegB family. These results suggest an unusual evolutionary trajectory of SegB
361 homologs.
362
363 Within the variable nucleotide sequences in the middle regions of the *segB* genes we
364 noticed an enrichment of $G[A]_n$ tracts of various lengths. Such sequences—for
365 example AAGAAGAAAAAGAAAAAG (Fig. 4a)—can form genomically unstable
366 regions, prone to slipped-strand mispairing. Because SegB homologs with sequences
367 longer than ~105-120 amino acids all contain insertions at this site, we propose that
368 the long SegB homologs arose from a short ancestor via progressive sequence
369 expansion at the $G[A]_n$ tracts. The SegB homologs of Metallosphaera species
370 represent an extreme example of this sequence expansion. These homologs have 82-
371 182 additional amino acids forming domains of unknown function. These domains
372 consist of 5-13 repeats of a Metallosphaera-specific 14-amino acid motif located
373 between the conserved SegA-binding and DNA-binding domains (Fig. 4a). The longer
374 homologs likely evolved from a shorter ancestor similar to the short homologs found
375 in other species of this family. Interestingly, in *M. javensis* and *M. sedula*, our search
376 revealed that multiple short and long copies of SegB may co-exist in the same species
377 (Fig. S5).
378

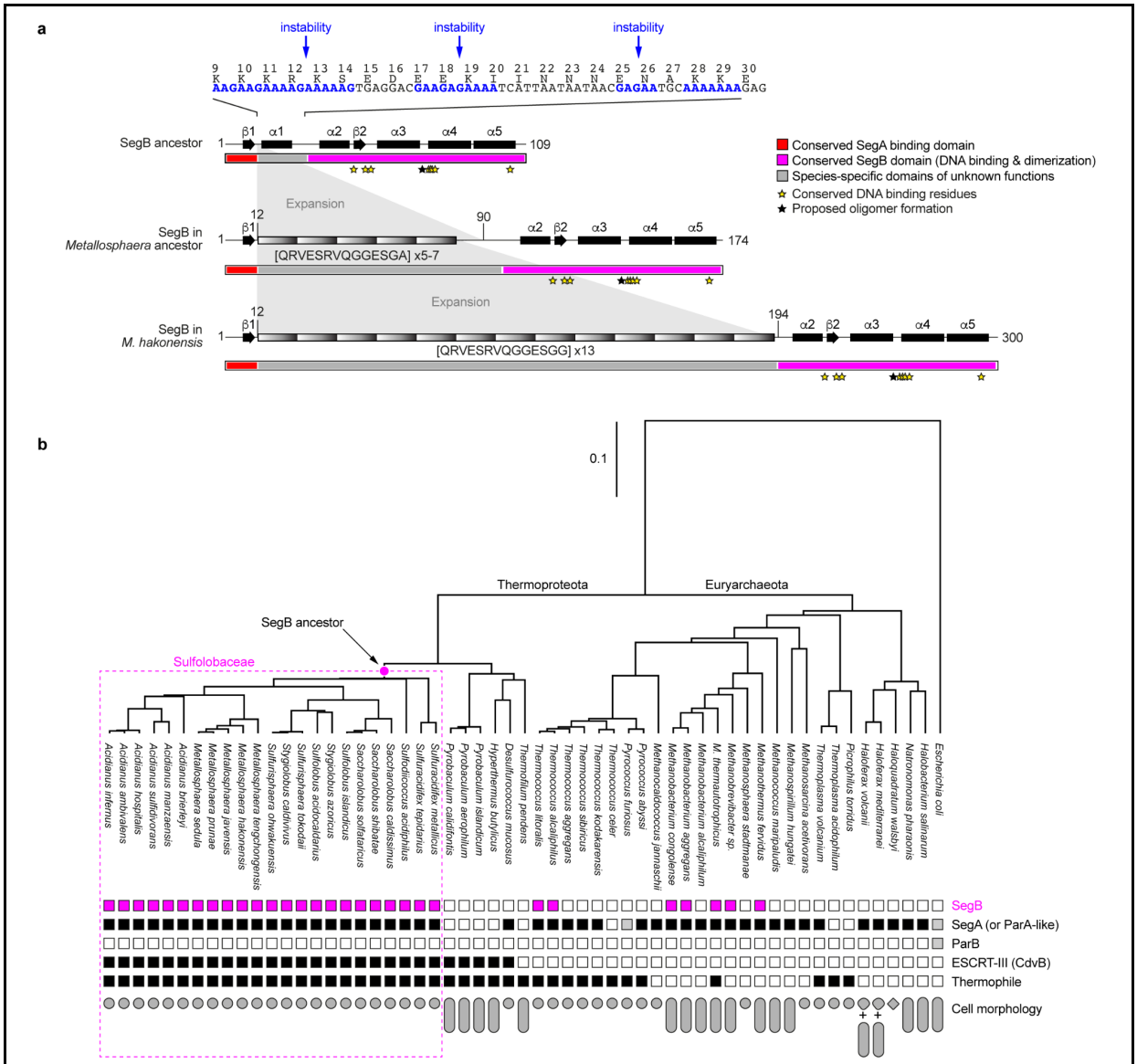

Figure 4. Evolution of SegB and shared characteristics of SegB-encoding archaea. a. Sites of species-specific domain insertions correspond to loci in *segB* 5' that contain GA and GAA repeats. The proposed SegB ancestor corresponds to a *Sso*-like short SegB. Insertion of additional domains at these sites in a species-specific manner may have led to longer SegB homologs in extant species such as in *M. hakonensis*. Conserved domains correspond to the C- and N-terminal parts of SegB and contain DNA- and SegA-binding residues. **b.** Comparative genomics suggests that SegB is involved in cell polarity in non-rod-shaped Thermoproteota. Compared to other groups, all SegB-encoding Thermoproteaota have in common to be non-rod-shaped thermophiles that seemingly rely on ESCRT-III for cell division and don't possess a homolog of bacterial ParB, suggesting that SegB is involved in the

391 establishment or the interpretation of polarity cues in non-rod-shaped cells, in lieu of
392 ParB which assumes a similar function in rod-shaped bacteria.
393
394 Mapping the length of all SegBs onto the natural phylogenetic tree of representative
395 Thermoproteota and Euryarchaeota species strongly suggested that the same
396 expansion mechanism can explain the lengths of all predicted SegB homologs (Fig.
397 4a). Since the majority of SegB sequences contain few (or no) extra domains between
398 the conserved N- and C-terminal domains, the common ancestor of all known SegBs
399 was short. SegB is present in all Sulfolobaceae, but absent from the rest of the
400 Thermoproteota (e.g. *Pyrobaculum* or *Desulfurococcus*), suggesting that SegB first
401 appeared in the common ancestor of Sulfolobaceae (Fig. 4b, Fig. S5). In eight families
402 of Sulfolobaceae, however, SegB homologs exhibit lineage-specific insertions of
403 additional domains of comparable lengths between the conserved N- and C-terminal
404 domains, likely corresponding to eight independent expansion events that yielded
405 SegB homologs with a high level of conservation among closely related species but a
406 relatively lower level of conservation overall (Fig. S5). The scarcity and low level of
407 conservation among SegB homologs in Euryarchaeota (especially in the conserved
408 N-terminal domain) suggests that these homologs were likely acquired by horizontal
409 gene transfer from Sulfolobaceae. More specifically, we propose that SegB was
410 transferred twice: once in the ancestor of *Thermococcus alcaliphilus* and *T. litoralis*,
411 and once in the ancestor of Methanobacteriales. These homologs evolved following a
412 similar expansion mechanism, yielding longer homologs containing lineage-specific N-
413 terminal domains of unknown function, or alternatively were lost (Fig. S5).
414
415 Our analysis suggests that SegB homologs of different lengths evolved via lineage-
416 specific addition of domains of unknown function between two highly conserved
417 ancestral domains. Since these seemingly diverse homologs were retained throughout
418 evolution, one wonders about the ancestral, conserved function of all SegBs.
419
420 **The phylogenetic distribution of SegB correlates with ESCRT-III proteins and**
421 **round cell morphology**
422 To identify a biological context that might have favored emergence and maintenance
423 of SegB as a component of the DNA segregation machinery, we looked for shared

molecular and cellular features common to the *segB*-encoding Sulfolobaceae but not shared with nearby clades. In addition to being non-rod shaped thermophiles, all Sulfolobaceae contain a CdvB (ESCRT-III) homolog involved in cytokinesis. (Fig. 5). The ancestor of extant Sulfolobaceae was, therefore, likely also a non-rod shaped thermophile that employed ESCRT-III for division. The correlation between rounded cell morphology and the presence of a *segB* gene suggested to us that SegB may help break symmetry and establish axes of chromosome segregation and division in cells that lack an obvious long axis.

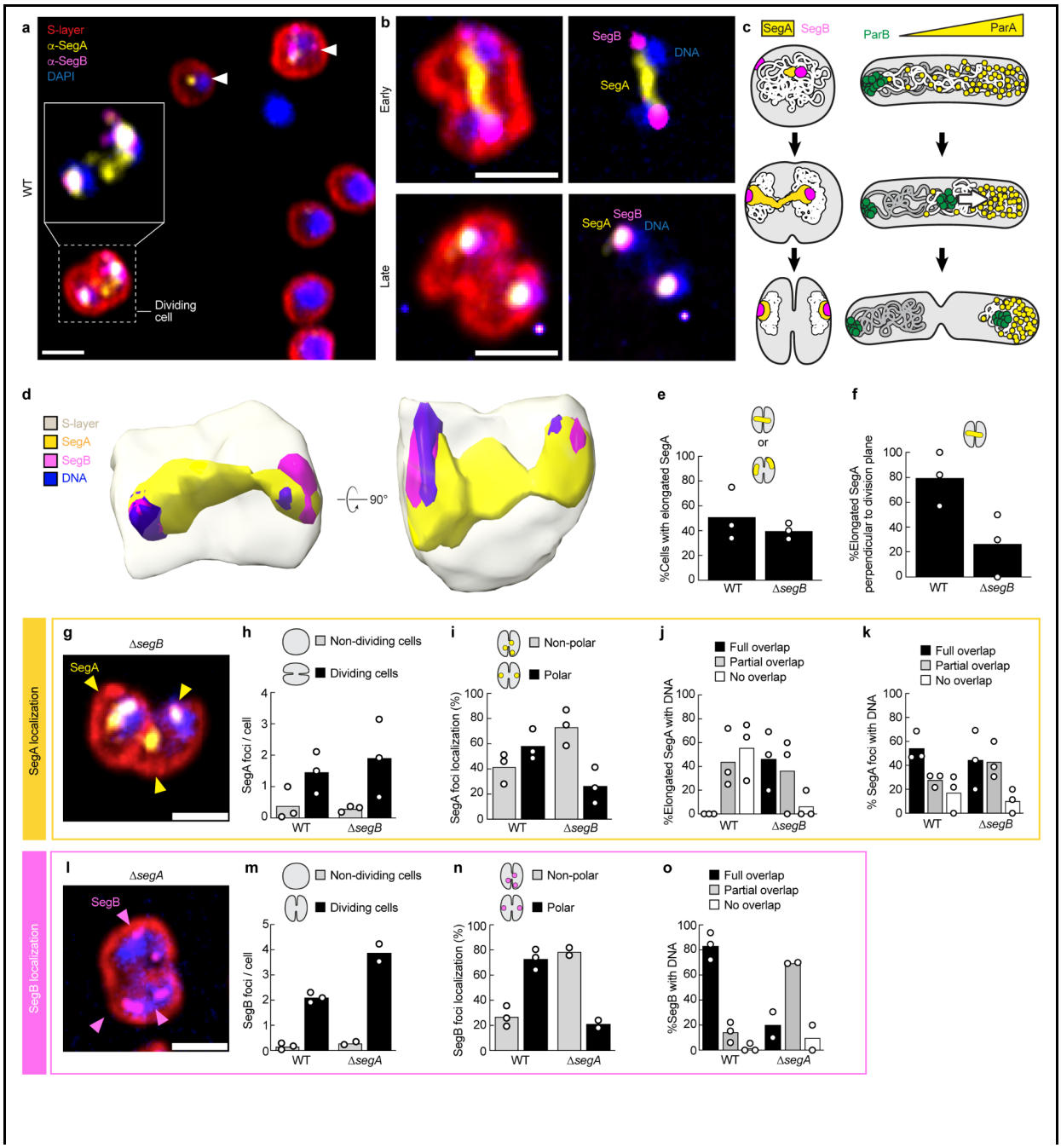

435 **Figure 5. Subcellular localization and function of endogenous SegA and SegB**
436 **in *Sulfolobus acidocaldarius*. a.** Representative example of the subcellular
437 localization of endogenous SegA (yellow) and SegB (magenta) in WT Saci obtained
438 by immunofluorescence, soft-embedding in agarose, super-resolution imaging and
439 deconvolution using specific antibodies. Chromosomal DNA was detected with DAPI
440 (blue), and the S-layer was covalently labeled with an amine-reactive Alexa Fluor 647
441 (red). The inset shows an enlarged view of a dividing cell where the S-layer signal was
442 removed for clarity. Arrowheads indicate non-dividing cells containing SegA and SegB
443 foci. **b.** In earlier stages of cell division, SegA is frequently seen as an elongated
444 structure stretching between two polar SegB foci and perpendicular to the division
445 plane. In later stages, SegA typically presents as discrete foci that fully overlap with
446 SegB and the DNA. **d.** Volumetric surface rendering of a *Saci* cell using ChimeraX
447 software. The SegA elongated figure is clearly seen to span the two chromosomes
448 and extend through the division plane. The gray cell surface was optimized using the
449 *midsurf* script in ChimeraX. **e, f**. Occurence and orientation of elongated SegA
450 structures in WT or in a strain of Saci where *segB* was deleted (Δ*segB*). **g.**
451 Representative example of the subcellular localization of endogenous SegB in Δ*segB*
452 and **(h-k)** corresponding quantification. **l.** Representative example of the subcellular
453 localization of endogenous SegB in Δ*segA* and **(m-o)** corresponding quantification. A
454 total of 161 (WT), 81 (Δ*segA*) and 109 (Δ*segB*) cells were analyzed; each dot
455 represents the mean of a biological replicate.
456
457 **SegAB forms a bipolar figure that links segregating sister chromosomes and**
458 **runs perpendicular to the plane of cell division**
459 We investigated the subcellular localization of SegAB in *S. acidocaldarius* by
460 generating antibodies against recombinant full-length SegA and SegB proteins from
461 *Saci* and performing super-resolution immunofluorescence microscopy. Cells were
462 soft-embedded in low-melt agarose to minimize mounting artifacts. Instantaneous
463 Structured Illumination Microscopy (iSIM) revealed that SegB forms two discrete foci
464 in 80% of all dividing cells that colocalize with segregated chromosomes, generally at
465 or near the cell poles (Fig. 5a, b, d). SegA exhibited multiple localization patterns
466 depending on whether the cell was early or late in the division process.
467

468 For quantitative analysis we separated images of dividing cells into Early and Late
469 Stages based on chromosome and S-layer morphology. We scored cells as Early-
470 Stage Division if they contained two compacted and clearly individuated
471 chromosomes, but exhibited only shallow ingression of the cell envelope. We scored
472 as Late-Stage Division cells containing two highly compacted, well-separated
473 chromosomes with a deep cleavage furrow ingression. Remarkably, ~50% of Early
474 Stage Division cells contained a bipolar SegA/SegB figure composed of a dense,
475 linear SegA structure capped at both ends by SegB foci. The SegA figure was
476 invariably aligned perpendicular to the plane of cell division and did not correspond to
477 an obvious underlying pattern of chromosomal DNA (Fig. 5a, c, d, Fig. S6). Volume
478 rendering unambiguously shows that SegA structures span the whole cell and connect
479 SegB foci from both cell poles (Fig. 5d). In 60% of Late Stage Division cells, SegA no
480 longer formed a single, linear figure, but two separated foci, often colocalized with the
481 separated SegB foci and chromosomal DNA at the cell poles (Fig. 5b). Less frequently,
482 we observed intermediate patterns, usually with SegA and SegB forming separate
483 puncta in Early-Stage Division cells, and overlapping/colocalized figures in Late-Stage
484 Division cells (Fig. S6). These SegA and SegB localization patterns differ dramatically
485 from those of ParA and ParB in rod-shaped bacteria (Fig. 5c) and point to
486 fundamentally different mechanisms of chromosome segregation.
487
488 **SegA consolidates SegB foci while SegB orients the divisional SegA figure**
489 To understand the specific functions of SegA and SegB we compared their localization
490 patterns in wildtype and mutant cells using super-resolution immunofluorescence
491 microscopy. In Δ*segA* cells, SegB no longer formed two discrete foci located at the
492 cell poles during division, but instead formed an average of four foci that no longer
493 localized to the cell poles and only partially overlapped chromosomal DNA (Fig. 5l, n).
494 In Late Stage Division cells lacking *segB*, SegA still formed dense filament-like figures
495 but they were less likely to be aligned perpendicular to the cell division plane (26% of
496 Δ*segB* cells compared to 80% of WT cells, Fig. 5f). These elongated SegA figures
497 were more strongly associated with chromosomal DNA (Fig. 6j). In Late Division Cells
498 the number of SegA foci was unchanged in Δ*segB* cells, but these foci failed to localize
499 to the cell poles. In both Δ*segA* and Δ*segB* deletion strains, chromosomal DNA
500 appeared less frequently compacted than in WT cells, and even appeared fragmented
501 in 27% and 15% of Δ*segA* and Δ*segB* cells, respectively, compared to 0% in WT cells

502 (Fig. 1e). In cells where chromosomal compaction appeared normal, it was less
503 frequently associated with the cell poles (only 57% and 69% in Δ*segA* and Δ*segB*
504 cells, compared to 83% in WT cells, Fig. 1f). We conclude from these experiments that
505 SegA and SegB drive chromosome segregation, but via a mechanism distinct from
506 that of ParAB in rod-shaped bacteria.

507 **Discussion**

508 Archaea are a phenomenally diverse but poorly understood domain of life. They are
509 ubiquitous: thriving in oceans, briny pools, hot springs, soil, and animal (including
510 human) microbiomes (Baker et al. 2020; Borrel et al. 2020; Duller and Moissl-Eichinger
511 2024; Hoegenauer et al. 2022). Archaea play an essential role in nitrogen and carbon
512 cycling, and they produce most of earth's atmospheric methane (Offre, Spang, and
513 Schleper 2013; Garcia, Gribaldo, and Borrel 2022). In addition to their ecological
514 significance, archaea also occupy a key position in the tree of life, as eukaryotes
515 appear to result from at least one fusion event between a bacterium and an archaeon
516 from the Asgard superphylum (Spang et al. 2015; Liu et al. 2021; Karki, Barth, and
517 Aylward 2024; Spang et al. 2018; Zaremba-Niedzwiedzka et al. 2017; Krupovic, Dolja,
518 and Koonin 2023; Eme et al. 2023; 2017).

519 Archaea share some chromosome segregation machinery with bacteria, especially
520 deviant Walker-box ATPases of the ParA family. Interestingly, some archaeal species
521 contain homologs of bacterial ParB proteins, while others appear to have innovated
522 new regulatory proteins to control ATP hydrolysis by ParA homologs. Previous work
523 in Sulfolobales identified two such archaea-specific regulators. The high copy number
524 plasmid, pNOB8, from *Sulfolobus* sp. strain NOB8H2, for example, encodes a
525 complete *parAB* operon, with ParA and ParB homologs that are ~37% and ~58%
526 identical to bacterial counterparts. This operon also encodes an additional, archaea-
527 specific protein, AspA, that mediates interaction between ParB and DNA (Schumacher
528 et al. 2015). The SegAB operon represents a more extreme case, in which ParB has
529 been replaced by either one (SegB) or two (SegB and SegC) archaea-specific factors
530 that regulate SegA activity and promote chromosome segregation.

531 We find that SegB is not simply "ParB with different letters" but a SegA effector that
532 facilitates an entirely different mechanism of chromosome segregation. Specifically,
533 SegAB in *S. acidocaldarius* promotes bipolar chromosome partitioning by a

534 mechanism distinct from that of ParAB-based systems in rod-shaped bacteria. For
535 example, the localization patterns of SegA and SegB during division are not consistent
536 with either the DNA relay model (Lim et al., 2014) or the observed distributions of ParA
537 and ParB in rod-shaped bacteria. In *Caulobacter*, ParA is depleted from regions
538 adjacent to ParB foci—especially from the region *between* segregating ParB/*parS*
539 complexes. Late in the segregation process, migrating ParB foci appear to chase the
540 ParA localization toward the distal pole. In contrast, SegA becomes highly
541 *concentrated* in the region between the separating SegB/*segS* complexes, forming a
542 dense, filament-like figure. The biophysical nature of this bipolar SegA/SegB figure is
543 unclear, but it reminds us of early reports that SegB-induced ATP hydrolysis causes
544 purified SegA to self-assemble into high order oligomers *in vitro* (Kalliomaa-Sanford
545 et al., 2012). In late stages of division, as the cleavage furrow ingresses, the dense
546 central SegA localization pattern splits in two and the separated halves retreat *toward*
547 the segregated SegB foci.

548 Comparing SegAB and ParAB localization patterns reveals a fundamental difference
549 in the functional relationships between the two sets of partner proteins. Rather than
550 providing a target for diffusing DNA/protein segregation complexes, our data suggest
551 that self-assembly of SegA either pushes chromosomes apart or prevents them from
552 remixing before division is complete. We are reluctant to speculate on the molecular
553 nature of the divisional SegA figure, but we note a couple of generic possibilities. SegA
554 might form linear protein polymers similar to ParM in bacteria (Garner et al., 2007;
555 Gayathri et al., 2012) or possibly a more amorphous phase condensate that is teased
556 into an elongated pattern by association with trace amounts of DNA that linger
557 between the segregating chromosomes. Interestingly, Kabli et al. (2025) recently
558 reported that SegA forms DNA-associated foci in non-dividing *Sa. solfataricus* cells, a
559 result consistent with our observations in *S. acidocaldarius*. These authors did not,
560 however, report results for dividing cells, so it remains to be seen whether *Sa.*
561 *solfataricus* SegA/SegB forms similar bipolar figures during division.

562 Regardless of the molecular nature of the bipolar SegA/SegB figures, their assembly
563 must be relatively rapid (<180 seconds). We deduce this from the fact that they appear
564 only during division—i.e. in cells with an obvious cleavage furrow. By live-cell, time-
565 lapse imaging the division process, from furrow initiation to final cell separation, takes

566 approximately 180 seconds, establishing this as an upper limit on the lifetime of the
567 bipolar SegA/SegB figures (Charles-Orszag et al., 2021).

568 During division, the SegB/*segS* complex appears to provide critical spatial information
569 required to align the entire bipolar SegA/SegB figure perpendicular to the plane of cell
570 division. The SegB/*segS* complex also appears to promote detachment of SegA from
571 the chromosome. We say this because loss of SegB does *not* prevent formation of an
572 elongated divisional SegA figure, but randomizes its orientation and results in more
573 spatial overlap between SegA and chromosomal DNA. Parham et al. (Parham et al.,
574 2025) recently reported evidence of spatio-temporal coordination between the SegAB
575 system and the ESCRT-III proteins that form the cytokinetic ring in Sulfolobales (Dobro
576 et al., 2013; Pulschen et al., 2020; Samson et al., 2008; Tarrason Risa et al., 2020).
577 We speculate that this coordination might underlie the SegB-dependent orientation of
578 divisional SegA figures (Fig. 5f).

579 SegA also contributes—directly or indirectly—to chromosome compaction in *S.*
580 *acidocaldarius*. In Sulfolobales, chromosome compaction occurs locally via the small
581 nucleoid associated proteins Alba, Cren7, and Sso7d (Cajili and Prieto, 2022; Laursen
582 et al., 2021); larger chromosome compartments are organized by the SMC-like protein
583 coalescin (Takemata et al., 2019; Takemata and Bell, 2020). In addition, in contrast to
584 the single origin of replication in bacterial chromosomes, the chromosome in
585 Sulfolobales contains three origins of replication (Lundgren et al., 2004) that are
586 believed to associate in the cell, in part due to the action of coalescin (Takemata et
587 al., 2019). It is possible that SegA may interact with these proteins. In any case, our
588 observations are consistent with other recent studies (Parham et al., 2025) and
589 suggest that chromosomal ParA-like proteins have evolved additional functions in
590 archaea. The DNA compaction activity in *Saci* SegA is important in that it seems to
591 promote formation of tightly focused SegB-DNA clusters, possibly to ensure
592 segregation of all three origins of replication at once. Loss of SegA causes the two
593 discrete foci of SegB observed in wildtype cells to fragment into multiple spots that fail
594 to find the cell poles. Our data, as well as other recent work (Kabli et al., 2025), reveals
595 that Saci SegB binds both a centromeric sequence *segS*, and more distal sites on the
596 chromosome. SegB cluster formation may be mediated by SegB disordered regions
597 in *Saci* that are known drivers of phase separation (Borcherds et al., 2021), or by
598 oligomerization, as residues proposed to promote oligomerization in *Sso* SegB are

599 conserved and solvent-exposed in *Saci* SegB. In other species, phase separation may
600 be promoted by the extensive N-terminal insertions. In any case, the concentration of
601 SegB into a single focus on DNA requires SegA.

602 Finally, loss of either SegA or SegB causes a growth defect in both *Saci* (this study)
603 and *Sso* (Kabli et al., 2025), but the genes encoding these proteins are not essential
604 in either organism. The same is true for *parAB* operons in many bacterial species,
605 such as *Deinococcus radiodurans*, *Vibrio cholerae*, *Bacillus subtilis*, *Pseudomonas*
606 *aeruginosa*, and *Mycobacterium smegmatis* (Charaka and Misra, 2012; Donovan et
607 al., 2010; Du et al., 2016; Jecz et al., 2015; Kadoya et al., 2011; Lee and Grossman,
608 2006; Lewis et al., 2002; Minnen et al., 2011; Santi and McKinney, 2015). Additional,
609 robust but cryptic DNA-segregation mechanisms must exist in both bacteria and
610 archaea. These mechanisms could involve either proteins specially adapted to
611 segregation or non-specific biophysical driving forces such as entropy or DNA looping
612 (Goloborodko et al., 2016; Harju et al., 2024; Jun and Wright, 2010). Regardless, it
613 appears that the ParAB and SegAB systems have evolved to employ similar ATPases
614 but different biophysical mechanisms to accelerate chromosome segregation, make it
615 more reliable, and/or coordinate it with cell division. Our work sheds light on the
616 diversity of mechanisms for ParA-based chromosome segregation, and may possibly
617 foreshadow additional species-specific differences—in other archaea but also in non-
618 rod-shaped bacteria where ParABS mechanisms are far from being completely
619 understood.

620 **Methods**

621 **Cell culture and preparation of conditioned media**

622 All *Sulfolobus acidocaldarius* strains were grown aerobically with agitation at 75°C in
623 Brock's media (Brock et al., 1972) supplemented with 0.1% tryptone, 0.2% dextrin and
624 10 ug.mL^{-1} uracil (Sigma-Aldrich). Conditioned Brock's media was prepared by
625 centrifugation of 50 mL of an exponentially growing culture (OD_{600nm} ~0.2-0.3) at 4,000
626 xg and room temperature for 15 min followed by filtration through a 0.22 µm filter to
627 remove cells and cell debris, and was stored at 4°C for up to a month. Cell growth of
628 WT and deletion strains was assessed by monitoring optical density at 600 nm.

629 **Construction of in-frame markerless deletion mutants in *S. acidocaldarius***
630 Knock-out strains were generated via the pop-in pop-out method described in (Wagner
631 et al., 2012). For the *segA* knockout, 557 bp upstream and 676 bp downstream of
632 *segA* were PCR amplified using primers 13461/13462 and 13463/13464, connected
633 via overlap PCR using primers 13461/13464, and cloned between the NotI and NdeI
634 sites of pSVA407, resulting in plasmid pSVA6463. For the *segB* knockout, 606 bp
635 upstream and 552 bp downstream of *segB* were PCR amplified using primers
636 13457/13458 and 13459/13460, connected via overlap PCR using primers
637 13457/13460, and cloned between the NdeI and BamHI sites of pSVA407 resulting in
638 plasmid pSVA6462. Plasmid transformation in the parental strain MW001 (referred to
639 as WT throughout the manuscript), initial selection via blue/white screening, secondary
640 selection, and mutant screening were performed as previously described. The
641 resulting deletion mutants MW1264 (Δ*segA*) and MW1263 (ΔsegB) were confirmed
642 by sequencing.
643
644 **Cloning and expression of recombinant SegA and SegB from *S. acidocaldarius***
645 All the sequences from *S. acidocaldarius* were codon optimized for expression in *E.*
646 *coli* and ordered as synthetic DNA fragments (Integrated DNA Technologies). The
647 fragment for His_6-KCK-SegA was ligated between the NdeI and NcoI sites of the pET-
648 22b(+) (Novagen) resulting in plasmid pACO29. The fragment for SegA-His_6 was
649 ligated between the NdeI and XhoI sites of the pET-22b(+) as in (Kalliomaa-Sanford
650 et al. 2012) resulting in plasmid pACO50. The gene fragments for SegB and $SegB_{S56C}$
651 were ligated between the SapI and XhoI sites of a N-His-ySUMO expression vector
652 (pTB146) resulting in plasmids pACO3 and pACO24, respectively. All constructs were
653 expressed in *E. coli* Rosetta2 cells. Expression was induced with 1 mM Isopropyl β-
654 D-1-thiogalactopyranoside (IPTG) when cultures reached OD_{600nm} ~2-3 and carried
655 out overnight at 16°C. Cells were lysed in a Microfluidizer LM10 (Microfluidics) in
656 respective His-tag binding buffers containing 1 mM phenylmethylsulfonyl fluoride
657 (PMSF) and a protease inhibitor cocktail (Roche). Lysates were clarified by
658 ultracentrifugation at 35,000 x*g* and the supernatants injected onto a HisTrap excel
659 column (Cytiva). His-tagged proteins were eluted with a gradient of 30 mM to 400 mM
660 imidazole. Protein-containing fractions were pooled and dialyzed overnight against
661 storage buffer. For SUMO-tagged proteins, the tag was removed by the addition of
662 yeast His_6-Ulp1 SUMO protease purified in-house overnight at 4°C during dialysing

663 into His-tag binding buffer. Both the tag and the protease were removed from the
664 protein mixture by passage onto a Ni-NTA agarose resin (Qiagen) by gravity followed
665 by gel filtration HiPrep 26/60 Sephacryl S100 HR column (Cytiva). For His_6-KCK-
666 SegA: His-tag binding buffer was 20% sucrose, 25 mM HEPES-KOH pH 7.4, 500 mM
667 KCl, 20 mM imidazole, 2 mM $MgCl_2$, 5 mM β-Mercaptoethanol (βME), 500 mM Mg-
668 ATP; elution buffer was 20% sucrose, 25 mM HEPES-KOH pH 7.4, 500 mM KCl, 400
669 mM imidazole, 2 mM $MgCl_2$, 5 mM βME, 100 mM Mg-ATP; storage buffer was 20%
670 sucrose, 25 mM HEPES-KOH pH 7.4, 500 mM KCl, 2 mM $MgCl_2$, 1 mM tris(2-
671 carboxyethyl)phosphine (TCEP), 100 mM Mg-ATP. For SegA-His_6: His-tag binding
672 buffer was 10% glycerol, 20 mM Tris-HCl pH 7.4, 300 mM NaCl, 20 mM imidazole, 2
673 mM $MgCl_2$, 500 mM Na-ATP, 5 mM βME; elution buffer contained 400 mM imidazole;
674 storage buffer was 10% glycerol, 20 mM Tris-HCl pH 7.4, 2 mM $MgCl_2$, 500 mM Na-
675 ATP, 2 mM TCEP. For all SegB constructs: binding buffer was 30 mM Tris-HCl pH 7.4,
676 250 mM NaCl, 30 mM imidazole, 5 mM βME; elution buffer was identical but contained
677 300 mM imidazole; dialysis/tag cleavage buffer contained 30 mM imidazole and 2 mM
678 TCEP; storage buffer 20% glycerol, 30 mM Tris-HCl pH 7.4, 250 mM NaCl, 2 mM
679 TCEP (note: all pH values provided correspond to pH at 4°C).
680
681 **Electrophoretic mobility shift assays (EMSA)**
682 For EMSAs, proteins were buffer exchanged in DNA binding buffer (10 mM Tris-HCl
683 pH 7.4, 50 mM KCl, 5 mM $MgCl_2$, 2.5% glycerol, 0.01% NP-40). Synthetic DNA
684 fragments (Integrated DNA Technologies) stocks were resuspended at 1 mM in
685 nuclease-free water. For DNA fragments larger than 50 bp, reaction mixes were
686 subjected to polyacrylamide gel electrophoresis in NuPAGE™ Bis-Tris Mini Protein
687 Gels, 4–12% (Invitrogen) in Tris-Glycine (TG) 1X buffer at 4°C. For DNA fragments
688 smaller than 50 bp, reaction mixes were subjected to 3% agarose gel electrophoresis
689 in Tris-borate-EDTA (TBE) 0.5X buffer at room temperature. DNA was stained with 1X
690 SYBR Gold and destained in either TG 1X or TBE 0.5X. Gels were imaged in a
691 ChemiDoc imager (BioRad).
692
693 **DNA curtain assays**
694 DNA curtains were established as previously described (Gallardo et al., 2015, Keenen
695 et al., 2021). Briefly, chrome features (or barriers) were nanofabricated on microscope
696 slides which were then converted to microfluidic flow-cells. Liposomes were used to

697 create a fluid lipid bilayer around chrome barriers on the surface of a flow-cell.
698 Biotinylated DNA from bacteriophage lambda (λ-DNA) was tethered to individual
699 biotinylated lipids via a multivalent streptavidin interaction. Buffer flow was then used
700 to align and extend tethered λ-DNA over chrome barriers to create visualizable DNA
701 curtains stained with the intercalating dye YOYO-1. A solvent-accessible cysteine was
702 introduced in SegB by point mutation (S56C), allowing cysteine labeling with Alexa
703 Fluor 569 C5 maleimide according to the manufacturer's instructions (Thermo Fisher
704 Scientific). $SegB_{S56C}$-AF568 (50% labeled) was injected into the flow-cell at 1μM in
705 imaging buffer containing 2 0mM Tris-HCl (pH 7.5), 50mM NaCl, 0.5mg/mL BSA, 0.5%
706 Pluronic F-127, 1 mM $MgCl_2$, 1mM DTT, and 10 pM YOYO-1. $SegB_{S56C}$-AF568 binding
707 to DNA was imaged at 0.1 Hz with a buffer flow rate of at least 0.5mL/min to maintain
708 DNA extension at chrome barriers. DNA curtains were imaged using total internal
709 reflection fluorescence (TIRF) microscopy, and images were captured with an EMCCD
710 camera run on Micro-Manager and Fiji. Binding distributions of $SegB_{S56C}$-AF568 were
711 measured in Python using analysis described previously (Ichino et al., 2021,
712 Strauskulage et al., 2023). Briefly, fluorescent channels were aligned and individual λ-
713 DNA molecules were identified in an image based on YOYO-1 signal. These
714 coordinates were used to identify $SegB_{S56C}$-AF568 binding events on DNA and two-
715 dimensional gaussians were fitted to determine the sub-pixel position of each
716 $SegB_{S56C}$-AF568 molecule. The relative base pair position of each $SegB_{S56C}$-AF568
717 binding event was calculated based on its distance from the free-end of the DNA using
718 the estimated extension of tethered, flow-extended λ-DNA. The mapped $SegB_{S56C}$-
719 AF568 binding distribution along λ-DNA was plotted alongside the distribution of
720 "AGNGT" binding sites identified using SeqIO from Biopython.
721
722 **Protein crystallization and structure determination**
723 SegB was used at a concentration of 11-18 mg/mL. Sitting drop vapor diffusion trays
724 were set up and incubated at room temperature, containing 0.4 μL drops of protein
725 and reservoir solution in a 1:1 ratio. Crystals formed after 35 days in 100 mM NH_4Cl
726 and 17-19% PEG 3350. Phases were determined by soaking crystals for 2 hours in a
727 solution consisting of mother liquor and 2 mM K_2PtI_6. Data was collected at ALS 8.3.1
728 on a Pilatus3 S 6M detector. Data indexing was completed using XDS and AIMLESS
729 in the CCP4 suite. Structure determination and refinement were done in the Phenix

730 programming suite. Visualization of SegB structure for figure preparation was done in
731 ChimeraX.
732
733 **Circular dichroism spectroscopy**
734 Circular dichroism spectroscopy was performed in a Jasco J715 spectrometer with 10
735 μM SegB in 10 mM potassium phosphate buffer pH 7.4. Buffer alone was used as a
736 blank. SegB secondary structure at 30°C was determined by measuring ellipticity from
737 200 nm to 280 nm. SegB thermostability was determined by measuring ellipticity at
738 222 nm while varying the temperature from 30°C to 110°C. SegB secondary structure
739 was determined again by lowering the temperature back to 30°C and measuring
740 ellipticity from 200 nm to 280 nm.
741
742 **Bioinformatic analyses**
743 Phylogenetic analyses were done in Geneious Prime (Biomatters Ltd.). A homology
744 search was performed in BLASTP against the nucleotide collection database (nr/nt)
745 using *Sa. solfataricus* SegB as query. Hits were manually filtered for duplicates or
746 poorly annotated sequences, yielding a final list of 72 hits. These sequences were
747 aligned with the Geneious Alignment tool, and a SegB homologs tree was built with
748 the Geneious Tree Builder using a Neighbor-Joining method to account for potential
749 differences in evolution rates between lineages. To map SegB homologs onto the
750 natural phylogenetic tree of archaea, fifty-seven 16s rRNA sequences were manually
751 retrieved from the National Center for Biotechnology Information (NCBI) database
752 corresponding to SegB-encoding and SegB-non-encoding Euryarchaea and
753 Thermoproteota archaeal species, and included the 16s rRNA sequence of
754 *Escherichia coli* as an outgroup. Sequences were aligned with the Geneious
755 Alignment tool and the tree was built with the Geneious Tree Builder using Unweighted
756 Pair-Group Method with Arithmetic Averaging (UPGMA). Known or predicted presence
757 or absence of ParA-like, ParB, and CdvB proteins in these 57 species was assigned
758 manually using available literature and NCBI BLASTP.
759
760 **Antibodies**
761 Polyclonal antibodies were raised against full-length recombinant tag-less SegB in
762 rabbit and His_6-KCK-SegA in guinea pig (Covance). Anti-SegB antibodies were further
763 affinity-purified against full-length SegB crosslinked to AminoLink Coupling Resin

764 (ThermoFisher) according to the manufacturer's instructions, and used at ~0.6 µg.mL-
765 1 (~1:1,000) for immunostaining. Anti-SegA was cleaned up by ultracentrifugation at
766 65,000 xg for 30 min and the supernatant used at 1:1,000. Secondary goat-anti-rabbit
767 AlexaFluor 488 antibodies and goat-anti-guinea pig AlexaFluor 568 antibodies
768 (ThermoFisher) were used at 1:1,1000. All antibodies were diluted in 3% bovine serum
769 albumin in phosphate buffered saline containing 0.05% Tween-20 (PBST-3% BSA).
770
771 **Immunostaining and soft embedding in low melting point agarose**
772 15 mL of exponentially growing cells (OD_{600nm} ~0.2-0.3) were collected by
773 centrifugation at 4,000 xg for 15 min at room temperature and the supernatant was
774 spared. Cells were then washed once in PBS 1X, resuspended in 225 µL PBS 1X and
775 added to a 1.5 mL microcentrifuge tube. The S-layer was labeled by adding 25 µL of
776 AlexaFluor 647-NHS-ester (ThermoFisher) freshly reconstituted at 0.5 mg.mL-1 in
777 anhydrous dimethyl sulfoxide (DMSO). Cells were incubated in the dark at room
778 temperature with gentle agitation for 20 minutes, after which they were centrifuged at
779 4,000 xg for 5 min, washed once with PBS 1X and once with non-pH-adjusted minimal
780 Brock media, and added back to the original culture supernatant in a culture flask and
781 allowed to grow for 1,5h. Cells were then collected by centrifugation at 4,000 xg for 15
782 min at 40°C, washed with prewarmed citrate buffer pH 3, and fixed stepwise in
783 increasing concentration of ice-cold ethanol according to (Cezanne et al., 2023). Fixed
784 cells were collected by centrifugation at 4,000 xg for 15 min at room temperature,
785 washed twice in PBS 1X, resuspended in 250 µL permeabilization buffer (GTET buffer:
786 50 mM glucose, 20 mM Tris pH 7.5, 10 mM EDTA, 0.2% Tween-20) and incubated in
787 the dark at room temperature for 20 min with gentle agitation. Permeabilized cells were
788 collected by centrifugation at 4,000 xg for 5 min at room temperature, rinsed three
789 times in PBS 1X, and blocked in 250 µL PBST-3% BSA overnight at 4°C. Anti-SegA
790 and anti-SegB antibodies were added and incubated for 1h at room temperature with
791 gentle agitation. Cells were washed four times in PBS 1X, resuspended in 250 µL
792 PBST-3% BSA containing fluorescently labeled secondary antibodies and 10 µg.mL-
793 1 4',6-diamidino-2-phenylindole (DAPI, ThermoFisher), incubated for 1h at room
794 temperature with gentle agitation, washed four times in PBS 1X and resuspended in 1
795 mL PBS 1X. 1-10 µL cells were added to 90 µL PBS 1X in wells of a 96-well glass
796 bottom plate (SensoPlate, Greiner BioOne) that was previously plasma treated, coated
797 with 0.01% poly-L-lysine (ThermoFisher) for 30 min at room temperature, washed with

798 MilliQ water and air-dried. The cell-containing plate was centrifuged at 1,000 xg for 2
799 minutes at room temperature. Cells were soft-embedded by slowly adding 100-150 µL
800 of a solution of 0.5% low melting point agarose (UltraPure LMP agarose, Invitrogen)
801 in 0.4% sucrose and 0.1M NaCl at 40°C after carefully discarding the supernatant.
802 LMP agarose was allowed to set at least 30 min at room temperature prior to imaging.
803
804 **Super-resolution fluorescence imaging**
805 Immunostained cells were imaged on a iSIM (Visitech) equipped with 405, 488, 561
806 and 647 nm lasers, a Nikon 100X 1.45NA PlanApo objective and a 1.5X optovar lens,
807 and a Hamamatsu Quest CMOS camera. Z-stacks were acquired with 0.125 µm steps.
808 Raw images were deconvolved with Microvolution in the Micro-Manager software
809 (Edelstein et al., 2010).
810
811 **3D volumetric surface rendering**
812 Even though the S-layer can be approximated to a 2D surface with virtually no depth
813 at the cellular scale, it appears as a ~200 nm-thick layer due to optical resolution
814 limitations. To facilitate interpretation of SegA and SegB subcellular localizations, we
815 developed a custom code in Python, *midsurf*, to recalculate the theoretical position of
816 the S-layer in ChimeraX (Goddard et al., 2018). This code moves surface vertices
817 along a volume gradient until they reach a maximum to find the center S-layer surface
818 in a roughly spherical shell (https://rbvi.github.io/chimerax-
819 recipes/middle_surface/midsurf.html).
820
821 **High-temperature live-cell imaging**
822 High-temperature live-cell imaging was done as in (Charles-Orszag et al., 2021).
823 Briefly, a DeltaT cell micro-environment control system (Bioptechs) was modified by
824 the manufacturer to allow it to reach temperatures up to 80°C. It was used on a Nikon
825 Ti-E inverted microscope equipped with a motorized stage. In order to enhance cell
826 attachment, the coverslips of the imaging chambers were modified with micropatches
827 of 0.8% gelrite (Gelzan, Sigma-Aldrich). The microscope objective was prewarmed to
828 65°C prior to imaging and kept at this temperature throughout the experiment. Upon
829 imaging, 500 µL of cells from an exponentially growing culture (OD_{600nm} ~0.2-0.3) were
830 added to an imaging chamber (final volume 2.5 mL) and allowed to settle for 15 min
831 at 75°C. The chamber controller was set to 78°C to maintain cells and media between

832 74.5 and 75.6°C throughout the experiment. A heated glass lid was used to prevent
833 condensation and evaporation. Differential interference contrast (DIC) microscopy
834 was performed with a green light-emitting diode illuminator (B180-RGB; ScopeLED)
835 through a Nikon 0.72NA CLWD air condenser, a Nikon PlanApo VC 100X 1.4NA oil
836 objective, Cargille 1809 immersion oil (refractive index ~1.515 at 65°C at 589nm), with
837 an additional 1.5X optovar lens, and a PointGrey CMOS camera (CM3-U3-50S5M-
838 CS). Cells were imaged with a 100-ms exposure every 5 seconds. All microscopy
839 hardware was controlled with Micro-Manager software (Edelstein et al., 2010).
840
841 **Data analysis**
842 Image analysis and quantifications were manually made in Fiji (ImageJ (Schindelin et
843 al., 2012)). Data was analyzed and graphs were prepared in Prism (GraphPad).
844 Figures and illustrations were prepared in Adobe Illustrator.
845
846 **Table 1. Plasmids used in this study**
847

Plasmid	**Description**	**Source**
pACO3	*Saci segB* gene (*saci0203*) codon optimized for expression in *E. coli*, ligated between SapI and XhoI sites of N-His-ySUMO expression vector (pTB146)	This study
pACO24	*Saci segB* gene (*saci0203*) containing a S56C mutation, codon optimized for expression in *E. coli*, ligated between SapI and XhoI sites of N-His-ySUMO expression vector (pTB146)	This study
pACO29	*Saci segA* gene (*saci0204*) codon optimized for expression in *E. coli*, with in frame N-terminal His_6 and KCK tags, ligated between the NdeI and NcoI sites of the pET-22b(+) (Novagen)	This study
pACO50	*Saci segA* gene (*saci0204*) codon optimized for expression in *E. coli*, with in frame C-terminal His_6,	This study

	ligated between the NdeI and XhoI sites of pET-22b(+) (Novagen)	
pSVA6462	*segB* deletion plasmid in *Saci*	This study
pSVA6463	*segA* deletion plasmid in *Saci*	This study

848

849 **Table 2. Primers used in this study**

Primer name	5'>3' sequence	Description
13457	GCATCATATGGTCCAATTCAATAATTCCTTCATTAGC	fw_US_KO_saci_0203 (*segB*), NdeI
13458	GATAGAAGGATGAGTGAGTAATGATATTACTATAATGAATATTACC	rev_US_KO_saci0203 (*segB*) overlap DS
13459	CATTATAGTAATATCATTACTCACTCATCCTTCTATCACC	fw_DS_KO_saci_0203 (*segB*) overlap US
13460	GCATGGATCCAGAGGGAAAAAAGGGAATATCCATTAGG	rev_DS_KO_saci_0203 (*segB*)
13461	GCATGCGGCCGCGGTTCTTGGGATCAAATTATTTAATGGTG	fw_US_KO_saci_0204 (*segA*), NotI
13462	GAGTCTATATATGAGTGAGTTAGACTTAATCTTAAACAGAAAAAAGAC	rev_US_KO_saci0204 (*segA*) overlap DS
13463	GATTAAGTCTAACTCACTCATATATAGACTCTTAACTCTATACCC	fw_DS_KO_saci_0204 (*segA*) overlap US
13464	GCATCCTAGGTCTAGAA	rev_DS_KO_saci_0204

	GTAGTGTAGAGAAAGCA GTG	(*segA*), NdeI

850

851 **Table 3. X-ray diffraction data and refinement statistics of SegB**

Wavelength	
Resolution range	58.32 - 1.85 (1.9 - 1.85)
Space group	P 21 21 21
Unit cell	44.944 54.296 116.634 90 90 90
Total reflections	162629
Unique reflections	25076 (1771)
Multiplicity	6.5
Completeness (%)	99.81 (99.94)
Mean I/sigma(I)	21.6
Wilson B-factor	31.13
R-merge	0.042
R-meas	0.05
R-pim	0.026
CC1/2	1
Reflections used in refinement	25076 (1771)
Reflections used for R-free	1999 (142)
R-work	0.3193 (0.3680)
R-free	0.3445 (0.4338)
Number of non-hydrogen atoms	2170
macromolecules	1994
ligands	0
solvent	176
Protein residues	244
Nucleic acid bases	n/a
RMS(bonds)	0.008
RMS(angles)	1.04
Ramachandran favored (%)	96.14
Ramachandran allowed (%)	3.86

Ramachandran outliers (%)	0
Rotamer outliers (%)	0.89
Clashscore	67.51
Average B-factor	32.35
macromolecules	31.97
ligands	n/a
solvent	36.64

852

853 **References**

854 Altschul, S.F., Gish, W., Miller, W., Myers, E.W., Lipman, D.J., 1990. Basic local alignment
855 search tool. Journal of Molecular Biology 215, 403–410.
856 https://doi.org/10.1016/S0022-2836(05)80360-2
857 Bandekar, A.C., Ramirez-Diaz, D.A., Palace, S.G., Wang, Y., Garner, E.C., Grad, Y.H., 2025.
858 Axial asymmetry organizes division plane orthogonality in Neisseria gonorrhoeae.
859 Current Biology S0960982225003094. https://doi.org/10.1016/j.cub.2025.03.024
860 Borcherds, W., Bremer, A., Borgia, M.B., Mittag, T., 2021. How do intrinsically disordered
861 protein regions encode a driving force for liquid–liquid phase separation? Current
862 Opinion in Structural Biology 67, 41–50. https://doi.org/10.1016/j.sbi.2020.09.004
863 Brock, T.D., Brock, K.M., Belly, R.T., Weiss, R.L., 1972. Sulfolobus: A new genus of sulfur-
864 oxidizing bacteria living at low pH and high temperature. Archiv. Mikrobiol. 84, 54–68.
865 https://doi.org/10.1007/BF00408082
866 Cajili, M.K.M., Prieto, E.I., 2022. Interplay between Alba and Cren7 Regulates Chromatin
867 Compaction in Sulfolobus solfataricus. Biomolecules 12, 481.
868 https://doi.org/10.3390/biom12040481
869 Charaka, V.K., Misra, H.S., 2012. Functional Characterization of the Role of the Chromosome
870 I Partitioning System in Genome Segregation in Deinococcus radiodurans. J Bacteriol
871 194, 5739–5748. https://doi.org/10.1128/JB.00610-12
872 Charles-Orszag, A., Lord, S.J., Mullins, R.D., 2021. High-Temperature Live-Cell Imaging of
873 Cytokinesis, Cell Motility, and Cell-Cell Interactions in the Thermoacidophilic
874 Crenarchaeon Sulfolobus acidocaldarius. Front. Microbiol. 12, 707124.
875 https://doi.org/10.3389/fmicb.2021.707124
876 Dobro, M.J., Samson, R.Y., Yu, Z., McCullough, J., Ding, H.J., Chong, P.L.-G., Bell, S.D.,
877 Jensen, G.J., 2013. Electron cryotomography of ESCRT assemblies and dividing
878 *Sulfolobus* cells suggests that spiraling filaments are involved in membrane scission.

879 MBoC 24, 2319–2327. https://doi.org/10.1091/mbc.e12-11-0785
880 Donovan, C., Schwaiger, A., Krämer, R., Bramkamp, M., 2010. Subcellular Localization and
881 Characterization of the ParAB System from *Corynebacterium glutamicum*. J Bacteriol
882 192, 3441–3451. https://doi.org/10.1128/JB.00214-10
883 Du, W.-L., Dubarry, N., Passot, F.M., Kamgoué, A., Murray, H., Lane, D., Pasta, F., 2016.
884 Orderly Replication and Segregation of the Four Replicons of Burkholderia
885 cenocepacia J2315. PLoS Genet 12, e1006172.
886 https://doi.org/10.1371/journal.pgen.1006172
887 Garner, E.C., Campbell, C.S., Weibel, D.B., Mullins, R.D., 2007. Reconstitution of DNA
888 Segregation Driven by Assembly of a Prokaryotic Actin Homolog. Science 315, 1270–
889 1274. https://doi.org/10.1126/science.1138527
890 Gayathri, P., Fujii, T., Møller-Jensen, J., Van Den Ent, F., Namba, K., Löwe, J., 2012. A Bipolar
891 Spindle of Antiparallel ParM Filaments Drives Bacterial Plasmid Segregation. Science
892 338, 1334–1337. https://doi.org/10.1126/science.1229091
893 Goddard, T.D., Huang, C.C., Meng, E.C., Pettersen, E.F., Couch, G.S., Morris, J.H., Ferrin,
894 T.E., 2018. UCSF ChimeraX: Meeting modern challenges in visualization and analysis.
895 Protein Science 27, 14–25. https://doi.org/10.1002/pro.3235
896 Goloborodko, A., Imakaev, M.V., Marko, J.F., Mirny, L., 2016. Compaction and segregation of
897 sister chromatids via active loop extrusion. eLife 5, e14864.
898 https://doi.org/10.7554/eLife.14864
899 Harju, J., Van Teeseling, M.C.F., Broedersz, C.P., 2024. Loop-extruders alter bacterial
900 chromosome topology to direct entropic forces for segregation. Nat Commun 15, 4618.
901 https://doi.org/10.1038/s41467-024-49039-w
902 Jecz, P., Bartosik, A.A., Glabski, K., Jagura-Burdzy, G., 2015. A Single parS Sequence from
903 the Cluster of Four Sites Closest to oriC Is Necessary and Sufficient for Proper
904 Chromosome Segregation in Pseudomonas aeruginosa. PLoS ONE 10, e0120867.
905 https://doi.org/10.1371/journal.pone.0120867
906 Jun, S., Wright, A., 2010. Entropy as the driver of chromosome segregation. Nat Rev Microbiol
907 8, 600–607. https://doi.org/10.1038/nrmicro2391
908 Kabli, A.F., Ng, I.W., Read, N., Pal, P., Reimann, J., Tran, N.T., Albers, S.-V., Le, T.B.K.,
909 Barillà, D., 2025. Coupling chromosome organization to genome segregation in
910 Archaea. https://doi.org/10.1101/2025.02.07.637068
911 Kadoya, R., Baek, J.H., Sarker, A., Chattoraj, D.K., 2011. Participation of Chromosome
912 Segregation Protein ParAI of *Vibrio cholerae* in Chromosome Replication. J Bacteriol
913 193, 1504–1514. https://doi.org/10.1128/JB.01067-10
914 Kalliomaa-Sanford, A.K., Rodriguez-Castañeda, F.A., McLeod, B.N., Latorre-Roselló, V.,
915 Smith, J.H., Reimann, J., Albers, S.V., Barillà, D., 2012. Chromosome segregation in

Archaea mediated by a hybrid DNA partition machine. Proc. Natl. Acad. Sci. U.S.A. 109, 3754–3759. https://doi.org/10.1073/pnas.1113384109

Laursen, S.P., Bowerman, S., Luger, K., 2021. Archaea: The Final Frontier of Chromatin. Journal of Molecular Biology 433, 166791. https://doi.org/10.1016/j.jmb.2020.166791

Lee, P.S., Grossman, A.D., 2006. The chromosome partitioning proteins Soj (ParA) and Spo0J (ParB) contribute to accurate chromosome partitioning, separation of replicated sister origins, and regulation of replication initiation in *Bacillus subtilis*. Molecular Microbiology 60, 853–869. https://doi.org/10.1111/j.1365-2958.2006.05140.x

Lewis, R.A., Bignell, C.R., Zeng, W., Jones, A.C., Thomas, C.M., 2002. Chromosome loss from par mutants of Pseudomonas putida depends on growth medium and phase of growth. Microbiology 148, 537–548. https://doi.org/10.1099/00221287-148-2-537

Lim, H.C., Surovtsev, I.V., Beltran, B.G., Huang, F., Bewersdorf, J., Jacobs-Wagner, C., 2014. Evidence for a DNA-relay mechanism in ParABS-mediated chromosome segregation. eLife 3, e02758. https://doi.org/10.7554/eLife.02758

Lin, M.-G., Yen, C.-Y., Shen, Y.-Y., Huang, Y.-S., Ng, I.W., Barillà, D., Sun, Y.-J., Hsiao, C.-D., 2024. Unraveling the structure and function of a novel SegC protein interacting with the SegAB chromosome segregation complex in Archaea. Nucleic Acids Research 52, 9966–9977. https://doi.org/10.1093/nar/gkae660

Livny, J., Yamaichi, Y., Waldor, M.K., 2007. Distribution of Centromere-Like *parS* Sites in Bacteria: Insights from Comparative Genomics. J Bacteriol 189, 8693–8703. https://doi.org/10.1128/JB.01239-07

Lundgren, M., Andersson, A., Chen, L., Nilsson, P., Bernander, R., 2004. Three replication origins in *Sulfolobus* species: Synchronous initiation of chromosome replication and asynchronous termination. Proc. Natl. Acad. Sci. U.S.A. 101, 7046–7051. https://doi.org/10.1073/pnas.0400656101

Lundgren, M., Bernander, R., 2007. Genome-wide transcription map of an archaeal cell cycle. Proc. Natl. Acad. Sci. U.S.A. 104, 2939–2944. https://doi.org/10.1073/pnas.0611333104

Minnen, A., Attaiech, L., Thon, M., Gruber, S., Veening, J., 2011. SMC is recruited to *oriC* by ParB and promotes chromosome segregation in *Streptococcus pneumoniae*. Molecular Microbiology 81, 676–688. https://doi.org/10.1111/j.1365-2958.2011.07722.x

Parham, J., Sorichetti, V., Cezanne, A., Hoogenberg, B., Foo, S., Kuo, Y.-W., Mawdesley, E., Daniels Gatward, L., Boulanger, J., Schulze, U., Saric, A., Baum, B., 2025. Temporal and spatial coordination of DNA segregation and cell division in an archaeon. To appear in bioRxiv.

Pulschen, A.A., Mutavchiev, D.R., Culley, S., Sebastian, K.N., Roubinet, J., Roubinet, M.,

953 Risa, G.T., van Wolferen, M., Roubinet, C., Schmidt, U., Dey, G., Albers, S.-V.,
954 Henriques, R., Baum, B., 2020. Live Imaging of a Hyperthermophilic Archaeon Reveals
955 Distinct Roles for Two ESCRT-III Homologs in Ensuring a Robust and Symmetric
956 Division. Curr Biol 30, 2852-2859.e4. https://doi.org/10.1016/j.cub.2020.05.021
957 Samson, R.Y., Obita, T., Freund, S.M., Williams, R.L., Bell, S.D., 2008. A role for the ESCRT
958 system in cell division in archaea. Science 322, 1710–1713.
959 https://doi.org/10.1126/science.1165322
960 Santi, I., McKinney, J.D., 2015. Chromosome Organization and Replisome Dynamics in
961 Mycobacterium smegmatis. mBio 6, e01999-14. https://doi.org/10.1128/mBio.01999-
962 14
963 Takemata, N., Bell, S.D., 2020. Emerging views of genome organization in Archaea. Journal
964 of Cell Science 133, jcs243782. https://doi.org/10.1242/jcs.243782
965 Takemata, N., Samson, R.Y., Bell, S.D., 2019. Physical and Functional Compartmentalization
966 of Archaeal Chromosomes. Cell 179, 165-179.e18.
967 https://doi.org/10.1016/j.cell.2019.08.036
968 Tarrason Risa, G., Hurtig, F., Bray, S., Hafner, A.E., Harker-Kirschneck, L., Faull, P., Davis,
969 C., Papatziamou, D., Mutavchiev, D.R., Fan, C., Meneguello, L., Arashiro Pulschen,
970 A., Dey, G., Culley, S., Kilkenny, M., Souza, D.P., Pellegrini, L., de Bruin, R.A.M.,
971 Henriques, R., Snijders, A.P., Šarić, A., Lindås, A.-C., Robinson, N.P., Baum, B., 2020.
972 The proteasome controls ESCRT-III-mediated cell division in an archaeon. Science
973 369, eaaz2532. https://doi.org/10.1126/science.aaz2532
974 Valdez, V.A., Neahring, L., Petry, S., Dumont, S., 2023. Mechanisms underlying spindle
975 assembly and robustness. Nat Rev Mol Cell Biol 24, 523–542.
976 https://doi.org/10.1038/s41580-023-00584-0
977 Wagner, M., van Wolferen, M., Wagner, A., Lassak, K., Meyer, B.H., Reimann, J., Albers, S.-
978 V., 2012. Versatile Genetic Tool Box for the Crenarchaeote Sulfolobus acidocaldarius.
979 Front Microbiol 3, 214. https://doi.org/10.3389/fmicb.2012.00214
980 Wurtzel, O., Sapra, R., Chen, F., Zhu, Y., Simmons, B.A., Sorek, R., 2010. A single-base
981 resolution map of an archaeal transcriptome. Genome Res. 20, 133–141.
982 https://doi.org/10.1101/gr.100396.109
983 Yen, C.-Y., Lin, M.-G., Chen, B.-W., Ng, I.W., Read, N., Kabli, A.F., Wu, C.-T., Shen, Y.-Y.,
984 Chen, C.-H., Barillà, D., Sun, Y.-J., Hsiao, C.-D., 2021. Chromosome segregation in
985 Archaea: SegA– and SegB–DNA complex structures provide insights into segrosome
986 assembly. Nucleic Acids Research 49, 13150–13164.
987 https://doi.org/10.1093/nar/gkab1155
988

Data availability

The atomic coordinates and structure factors have been deposited in the Protein Data Bank (https://www.rcsb.org/pdb) with PDB ID code 9OQF.

Acknowledgments

This work was supported by the National Institute of General Medical Sciences of the National Institutes of Health (R35-GM118119 to RDM), by the Howard Hughes Medical Institute Investigator Program (RDM), and by a Momentum grant (VW Foundation grant number 94993 to SVA). ACO has received support by the Simons Foundation as a Life Sciences Research Foundation fellow. NH was supported by a UCSF Pulmonary Division Training Grant (2T32HL007185), the Burroughs Wellcome Fund Postdoctoral Enrichment Program (1019894), and a University of California President's Postdoctoral Fellowship Program. We thank the X-ray Crystallography Facility at the University of California, San Francisco. We appreciate the use of Beamline 8.3.1 at the Advanced Light Source, which is supported by the University of California Office of the President MRPI program, Plexxikon Inc., and the Integrated Diffraction Analysis Technologies program of the US Department of Energy Office of Biological and Environmental Research. The Advanced Light Source (Berkeley, CA) is a national user facility operated by Lawrence Berkeley National Laboratory on behalf of the US Department of Energy under contract number DE-AC02-05CH11231, Office of Basic Energy Sciences. Molecular graphics and analyses performed with UCSF ChimeraX, developed by the Resource for Biocomputing, Visualization, and Informatics at the University of California, San Francisco, with support from National Institutes of Health R01-GM129325 and the Office of Cyber Infrastructure and Computational Biology, National Institute of Allergy and Infectious Diseases. The authors are particularly grateful to Jose De La Torre, Simonetta Gribaldo, Buzz Baum and Joe Parham, Daniela Barilla, Ethan Garner, Alex Bisson, Mecky Pohlschröder, Mullins lab members Justin Salat, Terri Lee, Jiongyi Tan, Natalie Petek, Kevin Nie, Wilson Nieves, Jessica Zhang, former students of the Physiology Course at the Marine Biological Laboratory, and former participants of the Archaeal Cell Biology Workshop, for years of fruitful discussions and technical help.

Contributions

A.C.O.: conceptualization, methodology, investigation, formal analysis, validation, visualization, figure preparation, writing original draft preparation, and review and editing. S.L.: methodology, formal analysis, validation, visualization, figure preparation, writing original draft preparation, and review and editing. N.H., L.S., A.B., B.W., M.V.W., G.A., A.F., T.G. & J.R.: conceptualization, methodology, investigation, formal analysis, validation, visualization, and editing. S. R., O.R., S.V.A. & R.D.M.: funding acquisition, supervision, methodology, investigation, formal analysis, writing original draft preparation, and review and editing. All authors contributed to the article and approved the submitted version.

Supplementary material

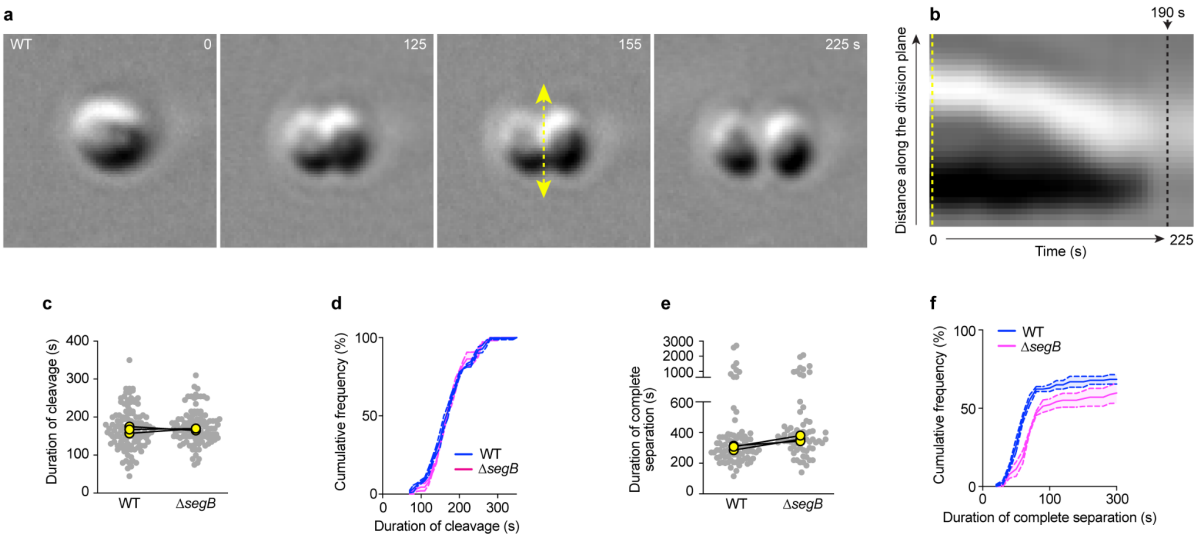

Figure S1. Live-cell imaging of cell division. a. Representative example of a dividing WT *S. acidocaldarius* cell imaged at 76°C using DIC. **b.** Kymograph showing the analysis of the duration of cleavage of the cytokinetic furrow. **c,d.** Duration of cleavage (time from the first invagination of the membrane to the point at which the cleavage is complete) and the time it takes the two daughters to fully separate for wildtype and *segB*-deletion mutant. Cells that were never observed to separate were excluded. Small gray dots represent each cell, while the large yellow dots are the medians of 3 independent biological replicates. **e,f.** Cumulative frequency distributions of all cells, including those that never separated. segB-deletion mutant cells exhibited a normal cleavage time, but then the daughters tended to stay connected longer. A slightly larger fraction of the *segB*-deletion cells never separated before the movies ended. Dark lines are the mean curves and light shading is the standard error of the mean from 3 biological replicates.

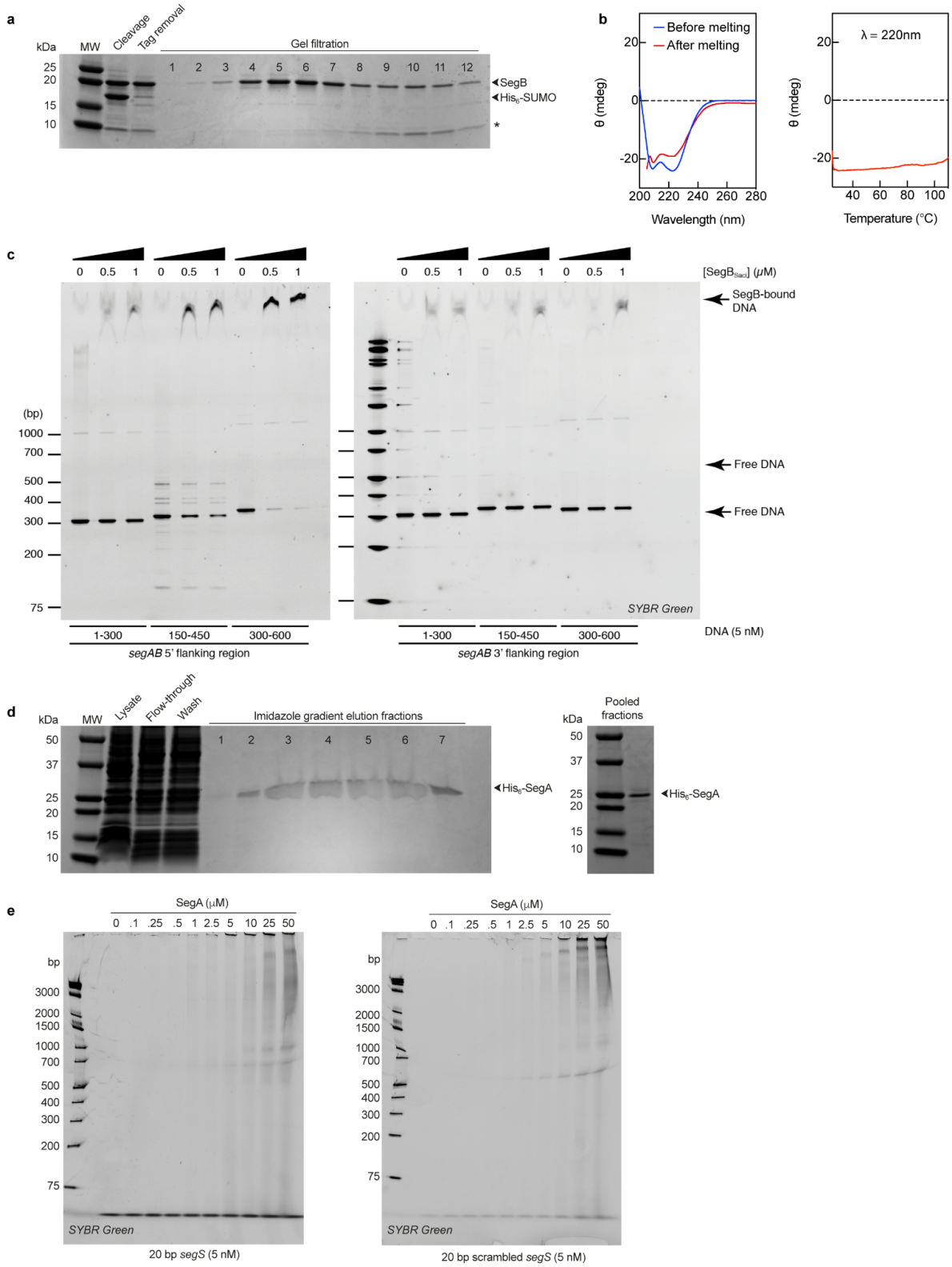

Figure S2. Protein purification, secondary structure determination of SegB, and DNA binding assays. a. Purification of SegB by gel filtration on a HiPrep 26/60 Sephacryl S100 HR column after nickel-affinity chromatography and enzymatic tag cleavage. **b.** Circular dichroism spectroscopy measurements of SegB ellipticity from

1053 220 nm to 280 nm before and after melting at 110°C, showing that SegB mostly
1054 consists of α-helices, and melting curve at 222 nm, showing that SegB remains folded
1055 at temperatures up to 110°C. **c.** Electrophoretic mobility shift assays (EMSAs) of SegB
1056 binding to DNA. Gels were stained for DNA using SYBR Green. (*Left*) SegB protein
1057 binds readily to the DNA matching the sequence of the region flanking the 5' of the
1058 *segAB* operon, which contains the *segS* sequence we identified. At the higher SegB
1059 concentrations, the amount of free DNA is reduced (right columns). (*Right*) SegB also
1060 binds nonspecifically to other DNA sequences, but not with as high an affinity, as
1061 indicated by the reduced shifted DNA. **d.** Purification of recombinant SegA-His_6. (*left*)
1062 Gel of the fractions eluted from a nickel-affinity column with imidazole. (*right*) Gel of
1063 pooled fractions showing purified SegA-His_6. **e.** EMSAs of SegA binding to DNA either
1064 with (*left*) or without (*right*) the specific *segS* sequence. Gels were stained for DNA
1065 using SYBR Green. Increasing SegA concentrations as shown across the top bind
1066 DNA in a monotonic manner, indicated by the DNA shift increasing from left to right.
1067 SegA binds equally to *segS* and scrambled *segS* sequences, indicating nonspecific
1068 DNA binding.

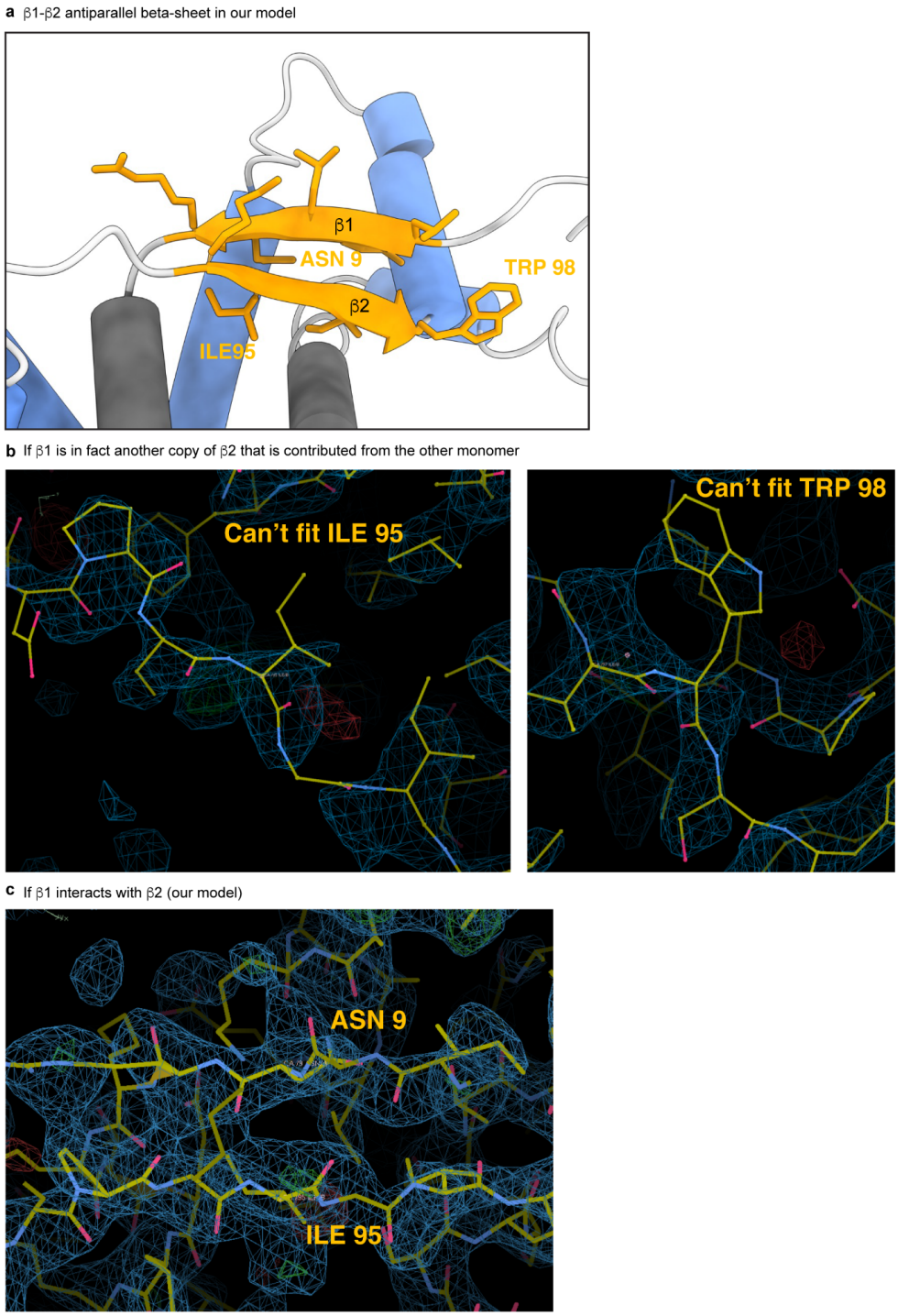

Figure S3. Details of the β-sheet region in SegB monomer. a. Detailed region of our crystal structure, which has two internal β strands stacking. The previously published structure of SegB from Sso had mirror β strand copies from two different monomers stacking to create the dimer interface. **b.** To test whether the stacking β strands are possibly from two different monomers, as seen in the previous structure, we examined the electron density of β1 in detail. If the β strands were mirror copies from different monomers, we would expect to see electron density from isoleucine 95

and tryptophan 98 from the same β sheet at the stacking region. But neither amino acid fits the observed electron density from our crystal structure data. **c.** Only asparagine from β1 and isoleucine 95 from β2 fit the electron density in the β stacking region, a sequence that corroborates our structural model that the two β strands are indeed internal to one monomer.

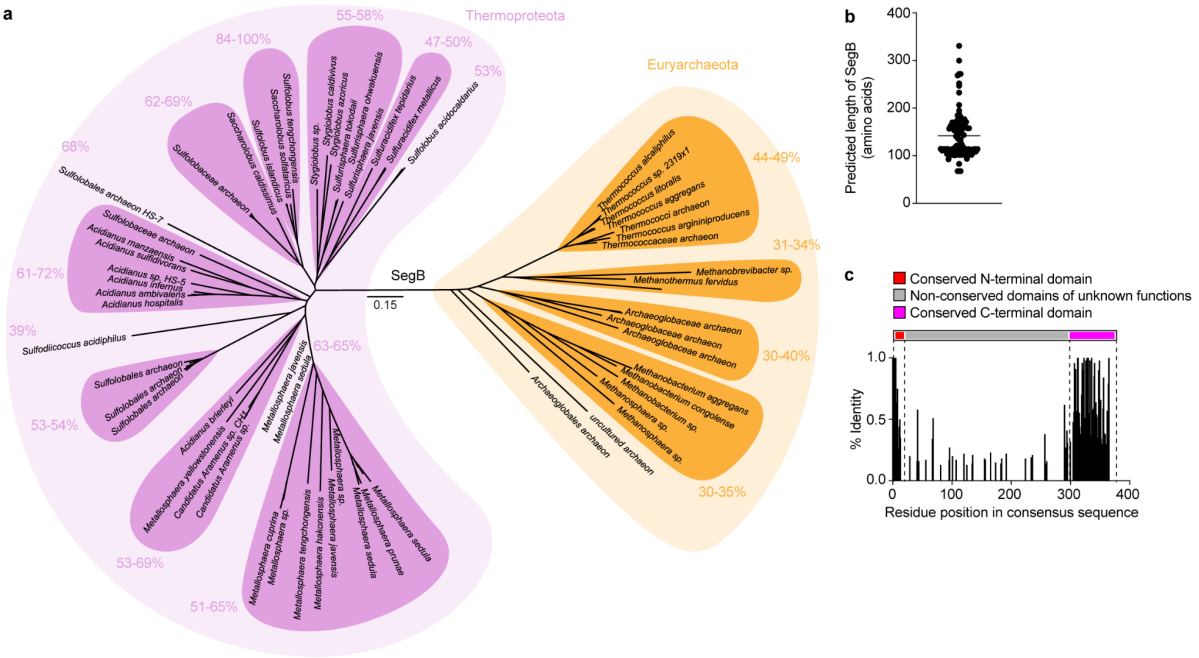

Figure S4. Distribution and conservation of archaeal SegB homologs. a. Phylogenetic tree of all archaeal SegB homologs identified. Numbers indicate sequence identity between selected sequence clusters and Sso SegB. **b.** Predicted amino acid length of all archaeal SegB homologs. **c.** Frequency of residue conservation in all archaeal SegB homologs compared to a consensus SegB sequence.

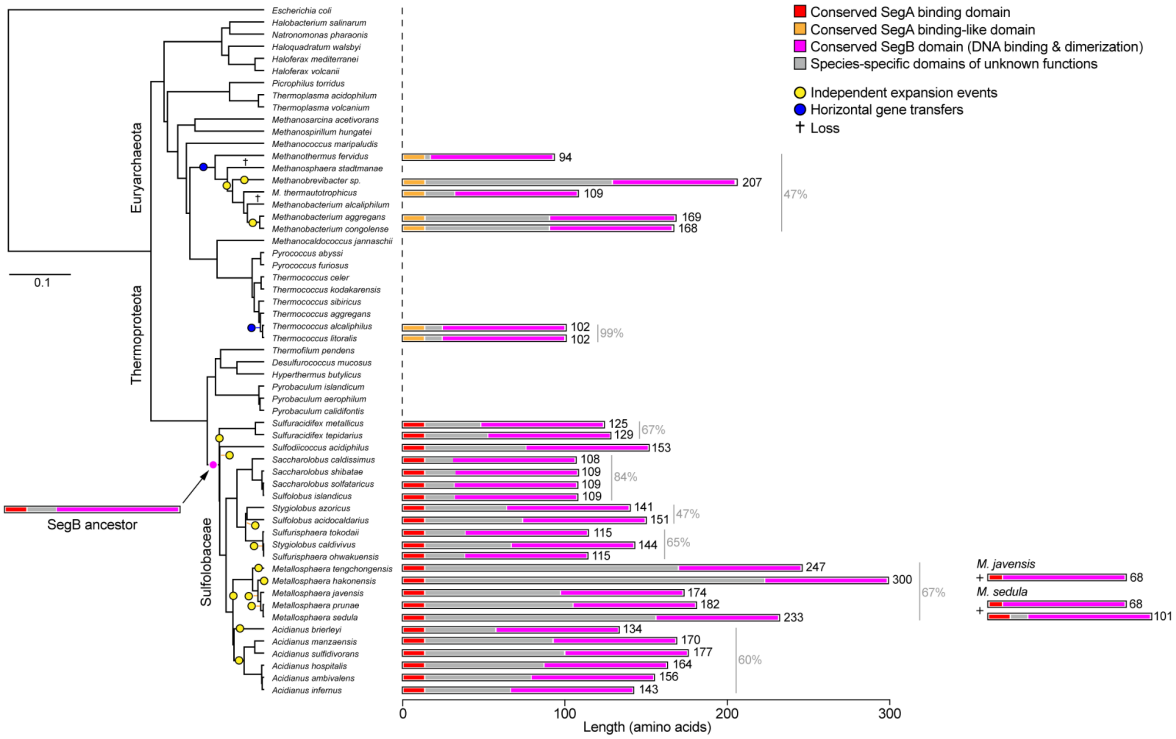

Figure S5. Mechanism for SegB sequence expansion and evolution of archaeal SegB. Mapping of SegB homolog lengths onto a phylogenetic tree of Thermoproteota and Euryarchaeota suggests that the ancestor of all SegB was likely a short homolog that was present in the ancestor of all Sulfolobaceae. At least eight independent occurrences of sequence expansion may have given rise to all SegB length variability in a lineage-specific manner (yellow circles). The presence of SegB in Euryarchaeota likely results from at least two horizontal gene transfers from Thermoproteota (blue circles). Numbers indicate sequence identity in selected SegB clusters.

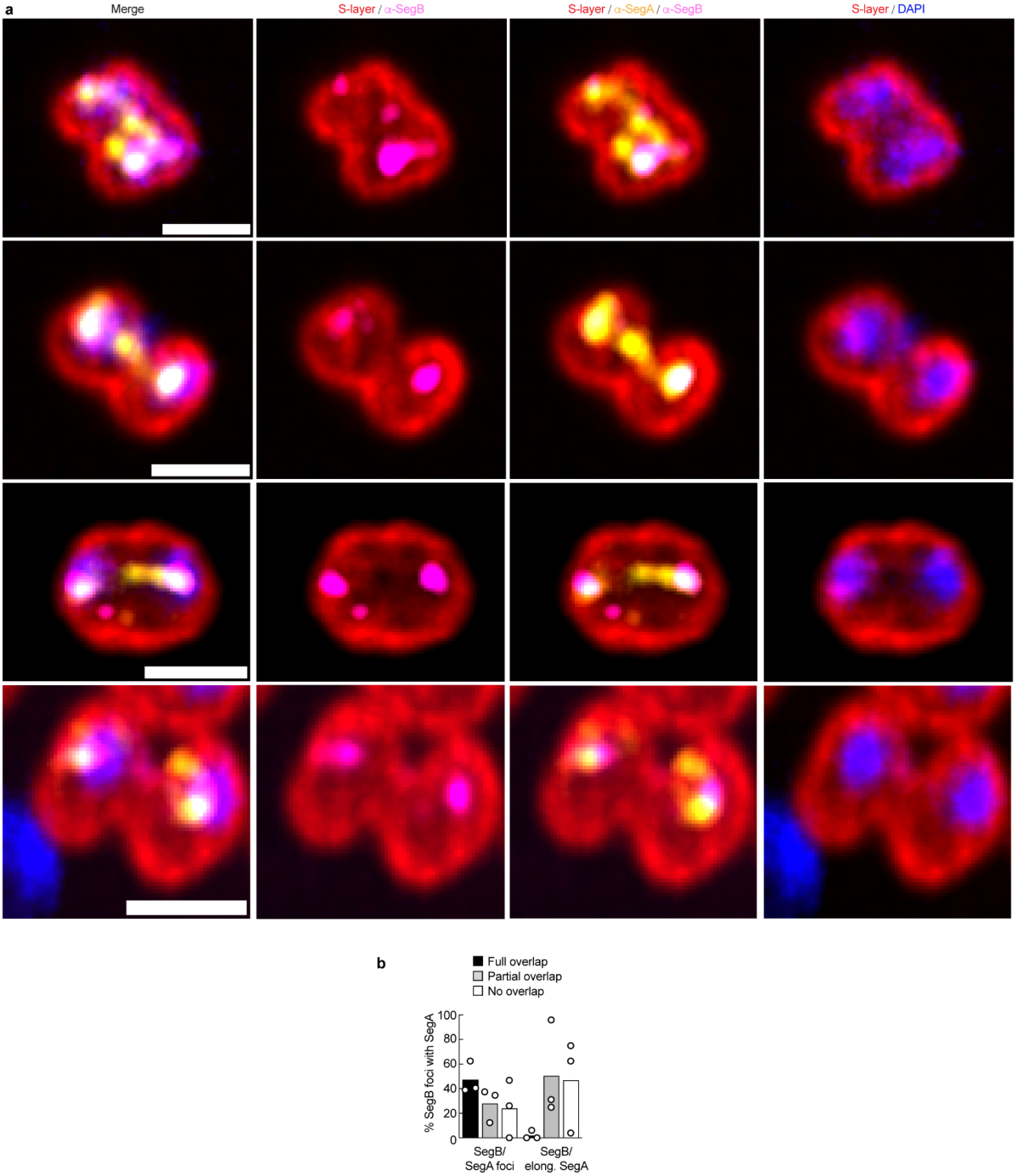

Figure S6. Subcellular localizations of SegA and SegB in dividing *S. acidocaldarius* (continued). a. Additional example immunofluorescence images of *Saci* cells with the S-layer, SegA, SegB, and DNA labeled. SegA forms multiple cellular distributions depending on the extent of division. Earlier in division (first and third row), SegA often forms puncta or extended structures near the division plane. Later in division (second and last rows), SegA tends to colocalize tightly with SegB and the

1116 compacted DNA. Scale bars are 1 μm. **b.** Quantification of the colocalization between
1117 SegB and SegA foci, or between SegB and elongated SegA figures.